Molecular properties of RmlT, a wall teichoic acid rhamnosyltransferase that modulates virulence in *Listeria monocytogenes*

Ricardo Monteiro[1,2,#,*],Tatiana B. Cereija[1,2,#], Rita Pombinho[1,2], Thijs Voskuilen[3], Jeroen D.C. Codée[3], Sandra Sousa[1,2], João H. Morais-Cabral[1,2,$] and Didier Cabanes[1,2,$,*]

[1] i3S – Instituto de Investigação e Inovação em Saúde, Universidade do Porto, Porto, Portugal

[2] IBMC – Instituto de Biologia Molecular e Celular, Universidade do Porto, Porto, Portugal

[3] Leiden Institute of Chemistry, Leiden University, The Netherlands

* Corresponding authors: didier@i3s.up.pt; ricardo.monteiro@i3s.up.pt

[#] These authors contributed equally

[$] These authors share last authorship

Abstract

Wall teichoic acids (WTAs) from the major Gram-positive foodborne pathogen *Listeria monocytogenes* are peptidoglycan-associated glycopolymers decorated by monosaccharides that, while not essential for bacterial growth, are required for bacterial virulence and resistance to antimicrobials. Here we report the structure and function of a bacterial WTAs rhamnosyltransferase, RmlT, strictly required for *L. monocytogenes* WTAs rhamnosylation. In particular, we demonstrated that RmlT transfers rhamnose from dTDP-L-rhamnose to naked WTAs, and that specificity towards TDP-rhamnose is not determined by its binding affinity. Structures of RmlT with and without its substrates showed that this enzyme is a dimer, revealed the residues responsible for interaction with the substrates and that the catalytic residue pre-orients the acceptor substrate towards the nucleophilic attack to the sugar. Additionally, the structures provided indications for two potential interaction pathways for the long WTAs on the surface of RmlT. Finally, we confirmed that WTAs glycosyltransferases are promising targets for next-generation strategies against Gram-positive pathogens by showing that inactivation of the RmlT catalytic activity results in a decreased infection *in vivo*.

18 **Introduction**

19 Infections caused by Gram-positive bacteria remain a major public health burden and a main
20 challenge in medicine. We witness the emergence of not only new pathogens but also new
21 bacterial strains with altered virulence properties and/or increased antimicrobial resistance [1].
22 Among them, *Listeria monocytogenes* is the Gram-positive foodborne pathogen that accounts
23 for the highest proportion of hospitalisation cases and number of deaths due to food poisoning
24 in Europe, with emergence of antibiotic resistances [1, 2]. The cell wall of *L. monocytogenes*
25 and other Gram-positive bacteria is a thick mesh-like complex that maintains cellular integrity.
26 It is composed of three major constituents, namely the peptidoglycan backbone, anionic
27 teichoic acid polymers and wall-associated proteins. Teichoic acids are the vast majority of cell
28 wall carbohydrates, either associated to the peptidoglycan (wall teichoic acids or WTAs) or
29 linked via a lipid anchor to the membrane in gram-positive bacteria (lipoteichoic acids or
30 LTAs) [3]. While the basic structure of LTAs remains relatively conserved among different
31 Gram-positive species and serovars [4-8], WTAs display significant structural and
32 constitutional diversity, as well as a variety of glycosylation patterns, resulting in different
33 fitness outcomes such as biofilm formation, virulence capacity and resistance to bacteriophages
34 and antimicrobials [4, 9-21]. WTAs are complex glycopolymers made of 20 to 30 repeating
35 units of ribitol-phosphate (RboP). In *Staphylococcus aureus*, the polymeric RboP backbone of
36 WTAs is modified through the addition of *N*-acetylglucosamine (GlcNAc) moieties by
37 different glycosyltransferases, including TarM, TarS, and TarP, which have different
38 specificities. While TarM is responsible for *α*-GlcNAc glycosylation at position *C*-4 of the
39 ribitol unit, TarS and TarP are required for the *β*-GlcNAc glycosylation at positions *C*-4 and
40 *C*-3, respectively [22-24]. Interestingly, all these individual GlcNAc additions to the poly-
41 RboP chain have a dramatic impact on pathogen-host interactions [25]. The molecular
42 properties of the *S. aureus* WTAs glycosyltransferases have been characterized [24-27].

43 *L. monocytogenes* WTAs are grouped in two subtypes: i) Type I WTAs, made of repeating
44 units of 1,5-phosphodiester-linked ribitol-phosphate glycosylated with GlcNAc at position *C*-
45 2 and rhamnose at position *C*-4 in serovar 1/2, with GlcNAc at position *C*-4 in serovar 3, or
46 non-glycosylated in serovar 7; and ii) Type II WTAs integrate a GlcNAc moiety into the
47 repeating unit at positions *C*-2 in serovars 4a, 4c, 5, 6b or at *C*-4 in serovars 4b, 4d, 4e, 4h and
48 6a in addition to other modifications with glucose, galactose or GlcNAc moieties, or with acetyl
49 groups [4, 20].

50 We previously performed the first genome-wide transcriptome of a bacterial pathogen infecting
51 a host organism using *L. monocytogenes* EGDe (serovar 1/2a) strain as model pathogen [28].

52 This study revealed that genes responsible for the biosynthesis of dTDP-L-rhamnose
53 (*rmlABCD*) and the transfer of the rhamnose moiety to WTAs (*rmlT*) are highly expressed
54 during *in vivo* infection [28]. Importantly, we showed that WTAs rhamnosylation is required
55 for the proper association of major virulence factors to the bacterial surface [14], and for
56 resistance to antimicrobial peptides [13] and antibiotics [16]. In addition, we showed that
57 WTAs decoration with rhamnose is strictly dependent on the rhamnosyltransferase RmlT [13].
58 Altogether, our previous data revealed that, although dispensable for bacterial growth, RmlT
59 has a significant impact on bacterial virulence and antimicrobial resistance.
60 Here, we explored the molecular properties of RmlT. Using a combination of structural and
61 biochemical approaches, we solved the structure of RmlT, uncovered its oligomeric
62 organization, identified the molecular determinants of donor-substrate binding and specificity,
63 and show that inactivation of RmlT catalytic activity can significantly reduce bacterial
64 virulence, confirming this rhamnosyltransferase as a promising target for new anti-virulence
65 strategies.

66 **Results**

67

68 **Enzymatic activity of the *L. monocytogenes* rhamnosyltransferase RmlT**

69 We previously showed that RmlT is required for WTAs rhamnosylation in *L. monocytogenes* [13].
70 To confirm that RmlT is indeed capable of transferring rhamnose to WTAs, we set-up an *in vitro*
71 enzymatic assay using dTDP-L-rhamnose, now on referred as TDP-rhamnose, as donor substrate and
72 naked WTAs as acceptor substrate. Naked WTAs were isolated from *L. monocytogenes* EGDe
73 Δ*rmlT*Δ*lmo1079* strain that lacks the ability to produce both RmlT and Lmo1079, respectively
74 reported to be involved in the addition of rhamnose and GlcNAc moieties to WTAs [13, 29]. RmlT
75 enzymatic activity was evaluated by analysing in parallel the reaction products: decorated WTAs and
76 TDP.

77 Decoration of WTAs was analyzed by electrophoretic mobility shift assay. After incubation with
78 TDP-rhamnose and purified RmlT, WTAs showed a change in migration, with bands running higher
79 in a native gel and displaying a more diffuse appearance compatible with glycosylated material
80 (Figure 1A). The generation of TDP by RmlT when transferring rhamnose to WTAs was quantified
81 indirectly using a coupled functional assay that measures the amount of free phosphate generated by
82 a phosphatase from the TDP produced by RmlT activity (Figure 1B). The amount of phosphate
83 detected in the reaction mixture containing TDP-rhamnose, WTAs and RmlT was significantly
84 higher than in the reaction mixture lacking RmlT. The generation of TDP only happens when naked
85 WTAs is present, showing that RmlT is not capable of hydrolysing TDP-rhamnose to TDP and
86 rhamnose in the absence of the acceptor substrate WTAs. Together, these experiments strongly
87 indicate that RmlT transfers rhamnose from TDP-rhamnose to naked WTAs, producing TDP and
88 rhamnosylated WTAs.

89

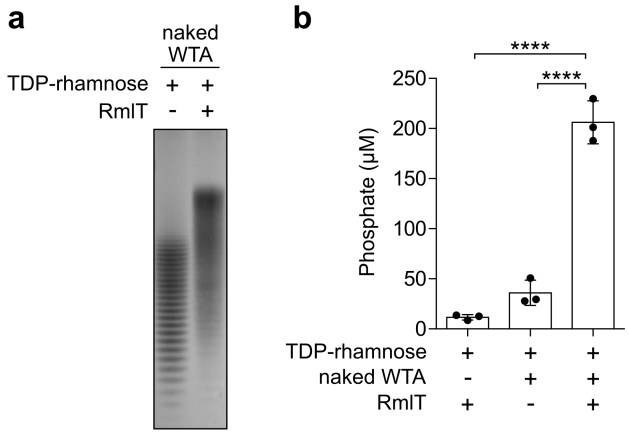

Figure 1: RmlT transfers rhamnose from TDP-rhamnose to naked WTAs. a) Electrophoretic mobility shift assay of the reaction mixture containing naked WTAs and TDP-rhamnose, in the absence (-) and presence (+) of RmlT. The individual bands observed in each lane correspond to different WTAs chains. **b)** Coupled functional assay quantifies the amount of phosphate released after hydrolysis of TDP molecules generated by RmlT. In both assays reactions ran for 60 minutes with 5 mM WTAs, 1 mM TDP-rhamnose and 10 µM RmlT. Mean ± SD (n = 3) and individual measurements are shown; one-way ANOVA; **** $p < 0.0001$.

Structure of RmlT

To gain insights into the molecular properties of *L. monocytogenes* RmlT, we determined the crystal structures of the full-length protein in different states at resolutions varying between 2.2 and 2.5 Å (Table 1). All the structures described below include multiple copies in the asymmetric unit. As assessed from the electron-density map, different copies display varying quality in different parts of the protein. Therefore, figures below show the best locally-defined protein copy, with its chain ID indicated in the legend. We also indicate the chain ID of the copy(ies) that is(are) globally the best defined (lowest average RSRZ value) in Table 1 and Supplementary Table 1.

The ~2.5Å crystal structure of RmlT in the apo state (PDB code: 8BZ4) presents the characteristic architecture of other WTAs glycosyltransferases like the *S. aureus* TarS and TarP [24, 27], with a catalytic region at the N-terminus and an oligomerization region at the C-terminus (Figure 2A and Supplementary Figures 1A and 2). Running from the N- to the C-terminus, RmlT shows a catalytic subdomain strongly connected to a helical subdomain, a large oligomerization subdomain and a turret subdomain (Figure 2A). Comparison between RmlT, TarS and TarP (all classified as members of the GT2 family of glycosyltransferases in CAZy, (http://www.cazy.org/), showed strong similarities at the level of the catalytic subdomains of the three enzymes (Figure 2B), while the helical, oligomerization and turret subdomains of RmlT are very similar to the equivalent regions in TarS (Supplementary Figure 1A) [27]. Interestingly, it has been shown that the oligomerization and turret

115 domains of TarS stand apart from the catalytic domain, adopting different dispositions that are
116 suggestive of flexibility [27]. In contrast, the oligomerization domain of RmlT lies over the catalytic
117 domain, establishing an extensive interaction surface (~480 $Å^2$) (Figure 2A and Supplementary
118 Figure 1A). In addition, the connection between the helical and oligomerization subdomains is
119 established in TarS by a 4 amino acid linker (residues 349-352) [27] while in RmlT three linkers
120 (residues 340-342, 368-388 and 406-410) run between the subdomains (Supplementary Figure 1B).

121 Contrasting with Tar proteins that form trimers (Supplementary Figure 1C) [27], RmlT eluted as a
122 dimer in a size-exclusion chromatography column (Supplementary Figure 3). Moreover, RmlT
123 assembles as a dimer in the crystal with the oligomerization subdomains interacting in an antiparallel
124 arrangement and positioning the catalytic subdomains at opposite corners of a rectangular shape
125 (Figure 2C). To assess the dimeric architecture of RmlT, we generated structure-guided mutants
126 ($RmlT_{Y368A+E372A}$ and $RmlT_{Y347A+Y368A+E372A}$) that aimed at disrupting the dimerization interface
127 (Figure 2C). Attempts to express and purify mutant proteins resulted in aggregated protein.
128 Nevertheless, after optimization of expression [30], we successfully purified a small amount of both
129 mutant proteins. By size exclusion chromatography, we showed that both mutant proteins elute as
130 monomers, confirming that mutated residues are part of the dimer interface and that wild type RmlT
131 is a dimer in solution (Supplementary Figure 3). Interestingly, mutations at the dimerization interface
132 did not affect the catalytic activity of RmlT *in vitro* (Supplementary Figure 3C). The impact of the
133 mutations at the RmlT dimerization interface was also tested *in vivo* using a bacteriophage rhamnose
134 binding protein (gp17), that specifically binds to rhamnose at the *L. monocytogenes* bacterial surface,
135 fused to GFP (gp17-GFP) [24]. Exponentially growing bacteria were incubated with gp17-GFP and
136 fluorescence associated with the bacterial cell wall staining was quantified in a microtiter plate format
137 and visualized by fluorescence microscopy (Figure 2D-E). Deletion of *rmlT* in the *L. monocytogenes*
138 EGDe strain resulted in a very significant decrease in the fluorescence intensity to background levels,
139 which was restored by complementation with *rmlT*, confirming the role of RmlT in the
140 rhamnosylation of the *L. monocytogenes* cell surface. Complementation with the *rmlT* dimerization
141 interface mutants significantly reduced, but did not abolish, fluorescence intensity (Figure 2D).
142 Fluorescence microscopy showed that the surface of bacteria expressing the dimerization mutants
143 (EGDe $\Delta rmlT::rmlT_{Y368A+E372A}$ and EGDe $\Delta rmlT::rmlT_{Y347A+Y368A+E372A}$) is still partially
144 rhamnosylated, consistent with their activity *in vitro*, but exhibited an altered pattern, with staining
145 restricted to the poles (Figure 2E). The mechanism underlying this change in staining pattern is not
146 known, but altogether these data demonstrate that RmlT is a dimer in solution and that changes in
147 dimer formation impact its physiological function.

148 **Table 1.** Data collection, phasing and refinement statistics.

	Apo SeMet-RmlT	Apo RmlT/ HEPES	RmlT/ UDP-glucose	RmlT/TDP-rhamnose	$RmlT_{D198A}$/TDP -rhamnose	RmlT/ 3-RboP	RmlT/ 4-RboP
PDB ID	**8BZ4**	**8BZ5**	**8BZ6**	**8BZ7**	**8BZ8**	9GZJ	9GZK
Diffraction data							
Space group	$P\ 2_1\ 2_1\ 2_1$	$P\ 1\ 2_1\ 1$	$P\ 1\ 2_1\ 1$	$P\ 1\ 2_1\ 1$	$P\ 1\ 2_1\ 1$	$P\ 2_1\ 2_1\ 2_1$	$P\ 1\ 2_1\ 1$
Cell dimensions							
a, *b*, *c* (Å)	83.4, 103.7, 178.4	82.1, 178.4, 92.2	85.5, 291.1, 89.8	87.0, 291.3, 92.4	87.4, 292.4, 93.1	83.2, 103.4, 178.6	86.3, 290.8, 91.0
α, β, γ (°)	90.0, 90.0, 90.0	90.0, 93.5, 90.0	90.0, 100.1, 90.0	90.0, 100.4, 90.0	90.0, 100.5, 90.0	90.0, 90.0, 90.0	90.0, 100.2, 90.0
Resolution (Å)	49.8 – 2.52	48.1 – 2.30	49.3 – 2.40	50.0 – 2.20	49.3 – 2.52	48.4 – 2.34	49.0 – 2.52
R_{merge}*	0.210 (1.735)	0.112 (1.295)	0.103 (1.560)	0.059 (1.087)	0.113 (1.394)	0.079 (1.363)	0.071 (1.053)
I / σI*	9.8 (1.5)	10.7 (1.4)	12.2 (1.3)	14.0 (1.2)	12.9 (1.6)	16.2 (1.2)	13.2 (1.4)
Completeness* (%)	100 (100)	99.2 (98.4)	99.1 (97.7)	99.8 (99.7)	100 (100)	99.9 (98.7)	99.5 (99.8)
Redundancy*	13.6 (13.3)	7.0 (7.2)	7.2 (7.3)	3.8 (3.6)	7.1 (7.1)	6.6 (6.0)	3.5 (3.5)
Refinement							
Resolution (Å)	49.8 – 2.52	48.1 – 2.30	44.2 – 2.40	50.0 – 2.20	45.8 – 2.52	41.6 – 2.34	42.9 – 2.52
No. reflections	53,011	115,974	166,253	227,111	153,926	65,950	147,192
R_{work} / R_{free}	0.219 / 0.251	0.193 / 0.220	0.195 / 0.235	0.187 / 0.215	0.191 / 0.228	0.192 / 0.226	0.198 / 0.232
Total No. atoms	9,848	20,336	30,490	30,744	30,233	9,962	29,353
Total No. water molecules	241	502	674	1,193	673	282	334
R.m.s deviations							
Bond lengths (Å)	0.003	0.004	0.004	0.005	0.002	0.003	0.002
Bond angles (°)	0.521	0.586	0.581	0.670	0.470	0.552	0.424
Ramachandran plot							
Favored (%)	95	96	96	97	97	96.58	95.69
Allowed (%)	5	4	4	3	3	3.42	4.31
Outliers (%)	0	0	0	0	0	0	0
Ligand	-	-	UDP-glucose	TDP-rhamnose	TDP-rhamnose	3-RboP	4-RboP
Molecules in the asymmetric unit	2	4	6	6	6	2	6
Best defined chain (Mean RSRZ)	A (0.04)	B (0.03)	E (0.15)	A (0.12)	A, C, D (0.04)	A (-0.32)	A, C, D, E (-0.17)
Residues NOT modeled (per chain)	A: M1-K17; B: M1-K20, E31-E33, G60-T65, K82-G90, G227-F234.	A: M1-N15, A228-S232; B: M1- K16, A228-F234; C: M1-N15; D: M1-K16; S87-W89; G227-S232.	All chains: M1-K17; B: also missing L623.	A: M1-K17, A228-S232; B: M1-K17, N230-F234; C: M1-K17, N230-G235; D: M1- K16, A228-G235; E and F: M1-K17, G227-F234.	A, C, D: M1-K17, N230-S232; B: M1-K17, A228-S232; E, F: M1-K17, G227-S233.	A: G0-N15; B: G0-D18, T30-G34, D58-Y66, K82-G90, G227-F234, L623.	A: G0-K16, A228-F234; B: G0-K17, A228-S232; C and D: G0-K17, G227-S233; E: G0-K17, G227-S231; F: G0-K17, T62-T75, A228-F234, L536-T545, L565-577, L596-V607, I619-L623.

149 *Values in parentheses are for highest-resolution shell.

150

151

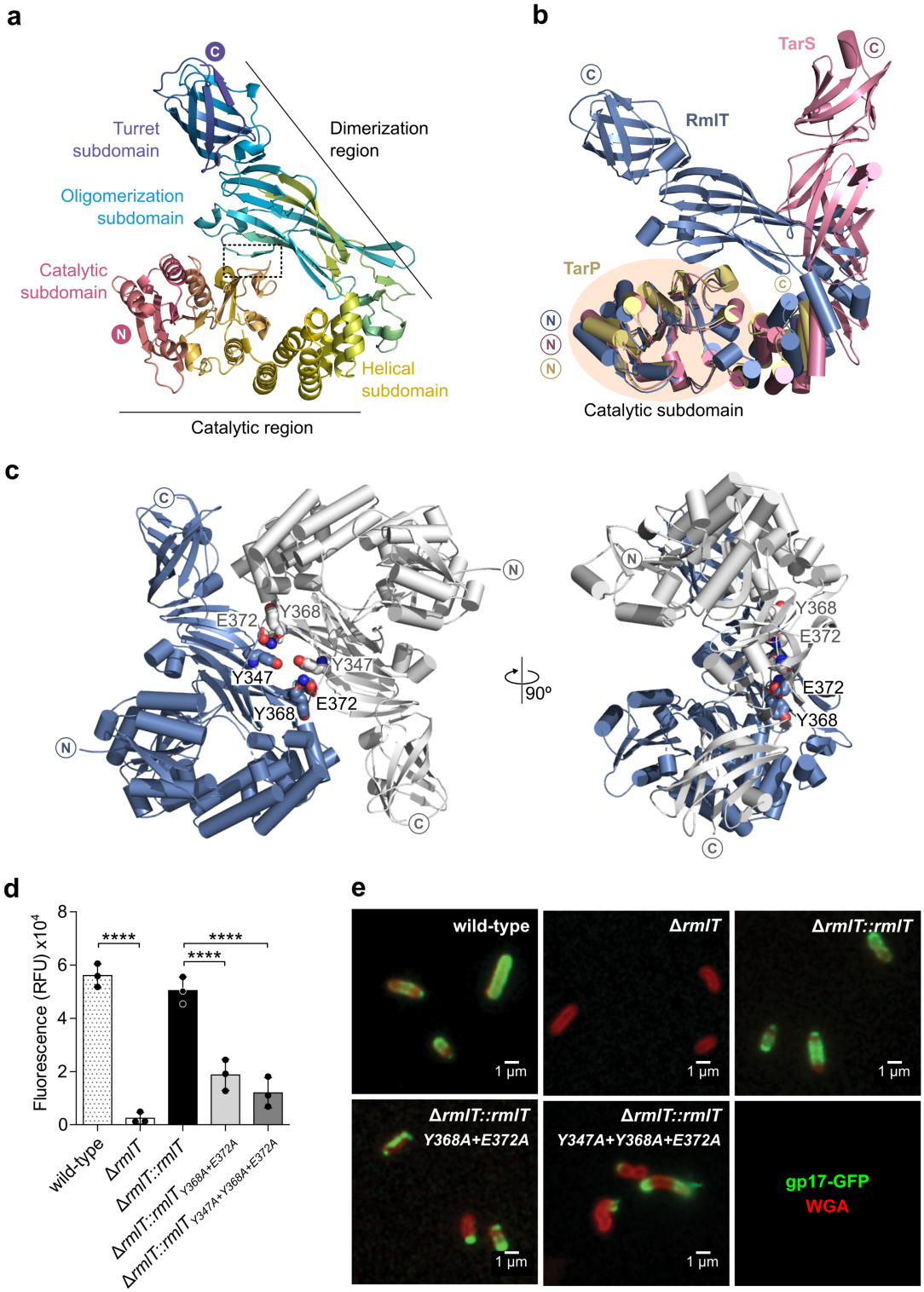

152 **Figure 2**: Structure of *L. monocytogenes* RmlT. **a)** Cartoon representation of a subunit of RmlT (PDB code: 8BZ4; chain
153 A) coloured from pink to purple, with subdomains and N and C termini indicated. Interaction between catalytic and
154 oligomerization subdomains is indicated by dashed rectangle. **b)** Superposition of RmlT (blue, PDB code: 8BZ4, chain
155 A) and *S. aureus* TarS [27] (pink, PDB code: 5TZ8) and TarP [24] (yellow, PDB code: 6H1J) through catalytic domain
156 (wheat ellipse) Cα atoms in helices h5, h6 and h11 (RmlT: residues 91-101, 118-130, 196-206; TarS: residues 72-82, 99-

111,176-186; TarP: residues 73-83; 100-112; 179-189) with RMSD values of 1.185 Å (TarS) and 0.886 Å (TarP). **c)** Two views of RmlT dimer showing subunits coloured blue and white and dimerization interface residues Y347, Y368 and E372 as spheres. **d)** Quantification of fluorescence associated with gp17-GFP bound to rhamnose at the surface of the *L. monocytogenes* wild-type EGDe strain and mutant strains EGDe Δ*rmlT::rmlT,* EGDe Δ*rmlT::rmlT*$_{Y368A+E372A}$ and EGDe Δ*rmlT::rmlT*$_{Y347A+Y368A+E372A}$. Mean ± SD (n = 3) and individual measurements are shown; one-way ANOVA, **** = $p < 0.0001$. **e)** Fluorescence microscopy images of *L. monocytogenes* cells stained with wheat germ agglutinin (WGA, red) and gp17-GFP (green) which binds to rhamnose at the bacterial surface.

RmlT active site

The structure of RmlT with bound TDP-rhamnose (PDB code: 8BZ7) was solved at 2.2 Å with 6 subunit copies in the asymmetric unit (Figure 3A, Table 1 and Supplementary Table 1). The electron-density for the ligand is clear and it was straightforward to build the nucleoside moiety in the catalytic subdomain (Supplementary Figures 4A-B and 5). However, there is a lack of detail in the electron-density for the sugar. The apparent spatial disorder of the sugar is evident in a superposition of the 6 copies of RmlT/TDP-rhamnose, while the nucleotide base and deoxyribose groups are unchanged between copies (Supplementary Figure 6A).

Comparison of catalytic subdomains of RmlT/TDP-rhamnose, TarP/UDP-GlcNAc (PDB code: 6H2N) [24] and TarS/UDP-GlcNAc (PDB code: 5TZE) [27] showed that many of the molecular interactions established by the nucleoside moiety of the donor substrate involve conserved residues (Supplementary Figures 2 and 6). In particular, in RmlT (Figure 3A) the nucleotide base is hydrogen bonded to D59 and N86, while the deoxyribose hydroxyl interacts with the main-chain carbonyl of the conserved P26 and amino group of H111. In addition, D112 and D113 together with the phosphate groups of the nucleotide are involved in the coordination of a single Mg^{2+}. D112 coordinates the cation directly while D113 interacts *via* two water molecules, just like in the other two enzymes (Supplementary Figure 6). The conserved residue D110 lines the bottom of the binding pocket by interacting with the also conserved R94. Of the interactions between the rhamnose and the protein, those involving E197 and D198 standout as these residues are conserved in TarP and TarS and are considered to be crucial for catalysis (Figure 3A and supplementary Figure 6) [24, 27]. In addition, two non-conserved tryptophans (W89 and W223) also interact with the sugar. The position of W89 varies between RmlT copies (Figure 3B) but that of W223 is invariant and is within hydrogen bond distance of the sugar oxygen (*O*1) (Figure 3B), raising the hypothesis that it contributes to the polarization of the anomeric carbon promoting the catalytic reaction.

In addition to the structures of apo-RmlT described above, with 2 copies in the asymmetric unit, and of RmlT/TDP-rhamnose complex (6 copies), we also determined another RmlT apo-structure with 4

copies per asymmetric unit (PDB code: 8BZ5) at a slightly higher resolution (2.3 Å) (Figure 3C, Table 1 and Supplementary Table 1). Globally, there are only minor changes between bound and unbound structures. Comparison between the donor binding sites of RmlT with and without TDP-rhamnose showed a widening of the binding site in the absence of the nucleotide (Supplementary Figure 7). The availability of multiple protein copies due to non-crystallographic symmetry and different crystal forms allowed us to explore in more detail the conformational space sampled in the two states. In the nucleotide-bound subunits there is little structural variability in the catalytic subdomain (Figure 3B). In contrast, we observed large spatial variability in the apo-structures (Figures 3D), likely to reflect local structural freedom due to the absence of stabilizing interactions with the ligand. In particular, the major structural variability in the catalytic subdomain occurs in two loops, loops A (residues 86-90) and B (residues 190-195). In one of the apo-protein copies, loop A (residues 86-90) flips away from the binding site and W89 (already described above as interacting with the rhamnose in the RmlT complex) points towards the bulk solvent.

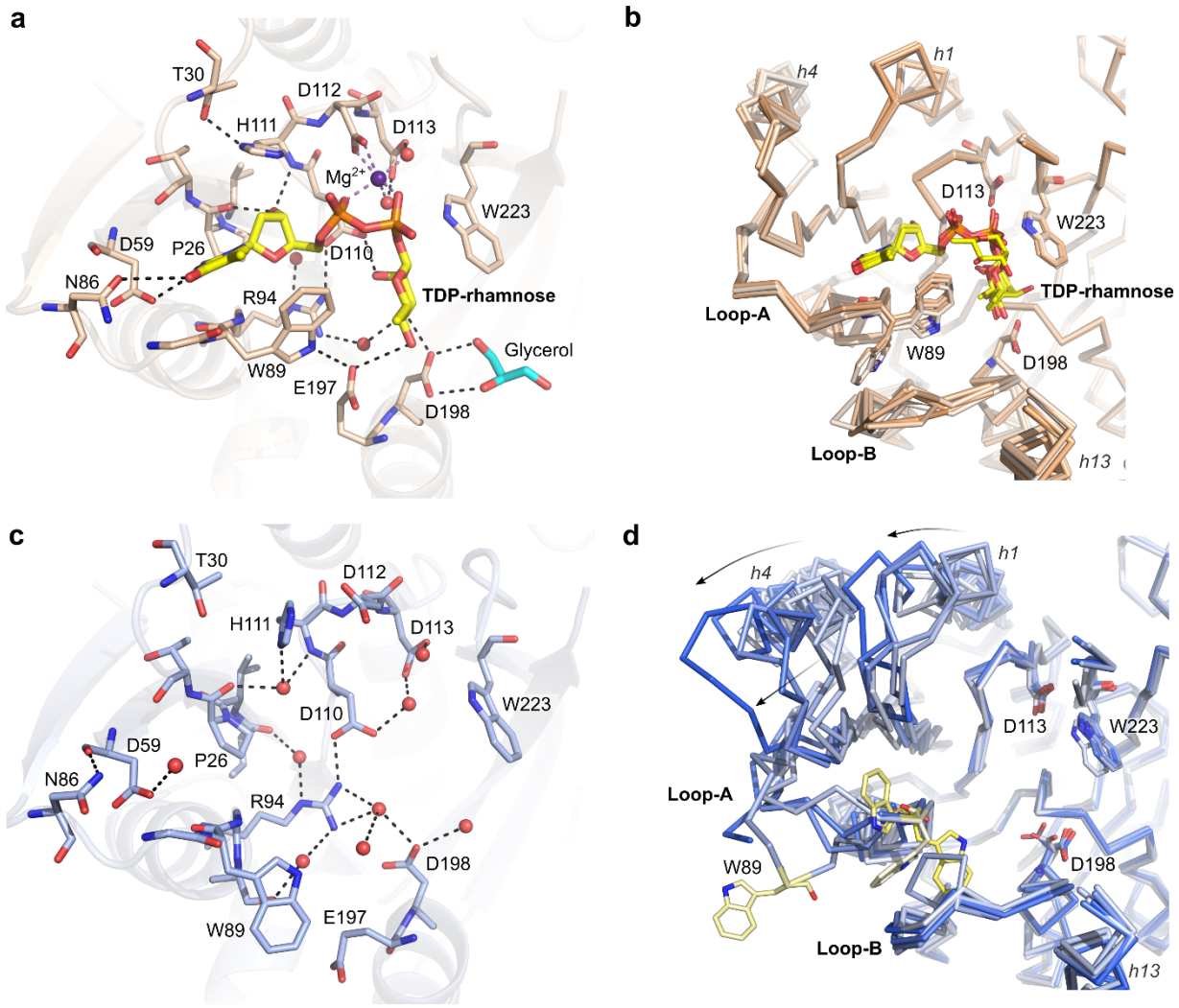

205 **Figure 3**: Active site of RmlT. **a)** Cartoon representation of the active-site region of RmlT with TDP-rhamnose and
206 interacting residues represented as sticks (PDB code: 8BZ7, chain D). Glycerol molecule used as cryo-protectant was
207 found interacting with D198, likely mimicking a ribitol molecule. Water molecules and Mg^{2+} are shown as red and purple
208 spheres, respectively. Hydrogen bonds and metal coordination are shown as black or light purple dashed lines. **b)**
209 Superposed active-sites (through residues 110 to 114) of RmlT/TDP-rhamnose copies (chains A to F) present in the
210 asymmetric unit, coloured in different shades of wheat (PDB code: 8BZ7). TDP-rhamnose and some substrate-interacting
211 residues are shown as sticks. RMSD relative to chain D: 0.034 Å (chain A), 0.046 Å (chain B), 0.027 Å (chain C), 0.042
212 Å (chain E) and 0.060 Å (chain F). **c)** Cartoon representation of the active-site region of the apo RmlT (chain A) with
213 donor substrate interaction residues represented as sticks (PDB code: 8BZ4). **d)** Superposed active-sites (through residues
214 110 to 114) of apo RmlT copies present in the asymmetric unit of two different crystal forms, coloured in different shades
215 of blue (PDB codes: 8BZ4 and 8BZ5). RMSD relative to chain A of 8BZ4: 0.966 Å (8BZ4 chain B), 0.319 Å (8BZ5
216 chain A), 0.229 Å (8BZ5 chain B), 0.070 Å (8BZ5 chain C) and 0.807 Å (8BZ5 chain D). Some substrate-interacting
217 residues are represented as sticks with W89 in yellow. Loops A and B and helices *h*1, *h*4 and *h*13 are indicated. Positional
218 variability of *h*1 and *h*4 is represented by arrows.

219

220 To evaluate the functional impact of some of the residues in the catalytic subdomain, we generated
221 single-point alanine mutants at the active-site residues E197, D198, W89 and W223 (Figure 3A).
222 Recombinant RmlT mutants were incubated with naked WTAs and TDP-rhamnose, and the reaction
223 was quantified by the free-phosphate coupled functional assay (Figure 4A). As expected, mutation
224 of E197 or D198 resulted in a complete loss of *in vitro* activity, fitting with their proposed role in
225 catalysis. W223A had wild-type levels of activity, showing that this residue is not important for the
226 catalytic reaction. In contrast, W89A resulted in a loss of function, supporting the idea that W89 has
227 a role in the proper positioning of the sugar.

228 To explore further the role of D198, which in TarS and TarP has been proposed to promote the
229 nucleophilic attack of the ribitol [24, 27], we determined the ~2.5 Å structure of the mutant
230 $RmlT_{D198A}$ in complex with TDP-rhamnose (PDB code: 8BZ8) (Figure 4B, Table 1 and
231 supplementary Table 1). The 6 copies of the protein in the asymmetric unit are occupied by nucleotide
232 and are for the most part identical to the structures of wild-type RmlT (Supplementary Figures 4C-
233 D, 5B and 8). In the $RmlT_{D198A}$ mutant structure the sugar is even less defined in the electron-density
234 and appear to have moved away in all 6 copies of the asymmetric unit from its position in the wild
235 type protein (Figure 4B and Supplementary Figures 4C, 4D, 6B and 9). This suggests that D198 has
236 a role in positioning the sugar, in agreement with the observation of contacts with the rhamnose in
237 the RmlT/TDP-rhamnose structure.

238 We also evaluated *in vivo* the impact of mutants for residues in the catalytic subdomain. The *L.*
239 *monocytogenes* EGDe Δ*rmlT* strain was complemented with wild-type RmlT or RmlT mutants

240 (RmlT$_{W89A}$, RmlT$_{E197A}$, RmlT$_{D198A}$, and RmlT$_{W223A}$), and the effect of each mutation was analyzed
241 using the gp17-GFP rhamnose binding protein. Mutations of W89, E197 and D198 completely
242 abolished rhamnose from the bacterial surface (Figures 4C-D), confirming their importance for RmlT
243 activity. Surprisingly, W223A also induced the absence of surface rhamnosylation, which suggests
244 that the mutation affected a property of RmlT that is specific to its physiological function *in vivo*
245 other than catalytic reaction.

246

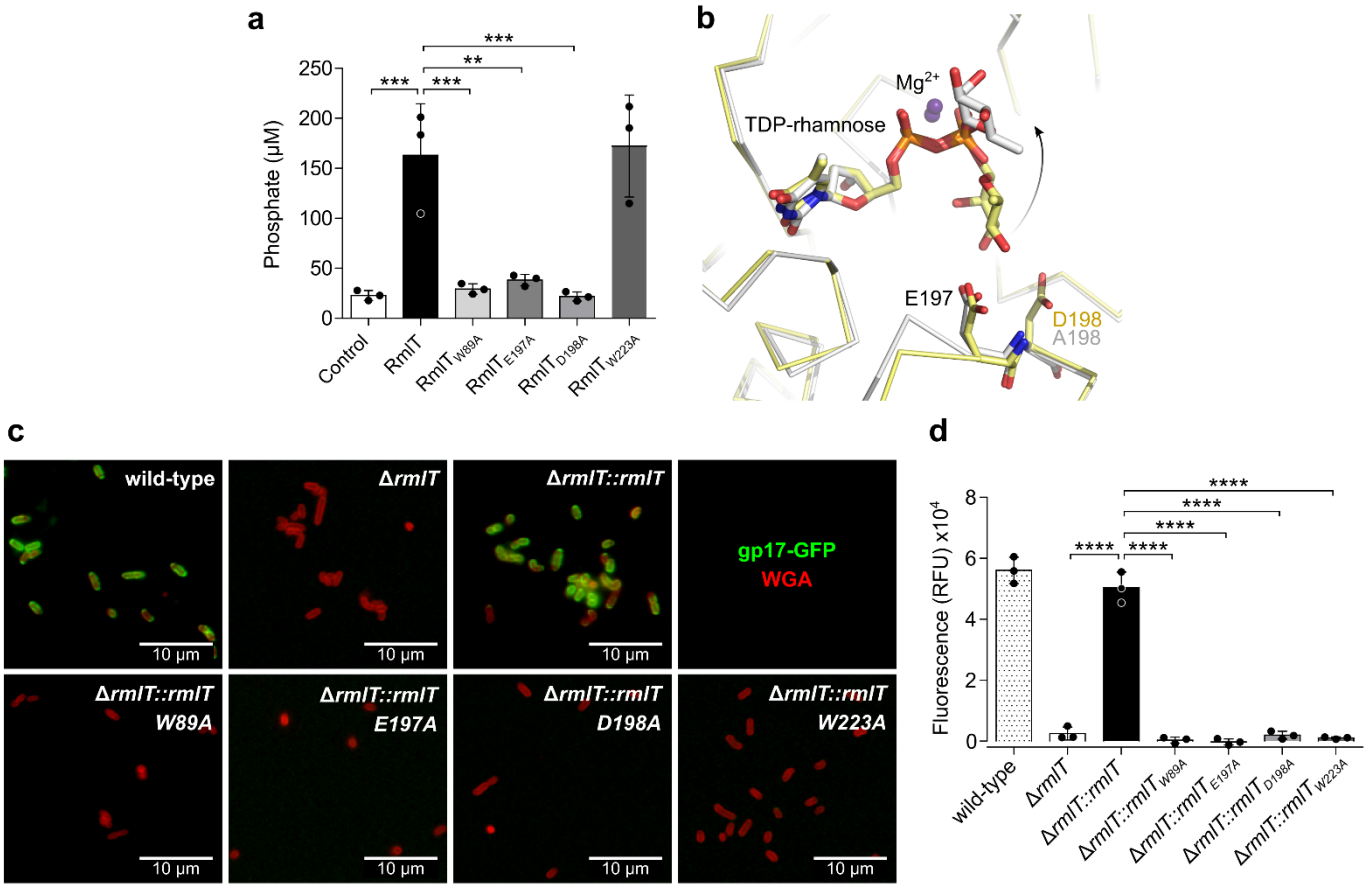

247

248 **Figure 4**: Impact of active-site residues in RmlT activity. **a)** Quantification of the amount of phosphate released from the
249 product generated by RmlT, RmlT$_{W89A}$, RmlT$_{E197A}$, RmlT$_{D198A}$ and RmlT$_{W223A}$. Phosphate was quantified after 30 minutes
250 reaction from mixtures containing 1 mM naked WTAs, 200 µM TDP-rhamnose and 2 µM protein. **b)** Superposition of
251 active-sites of RmlT (light yellow, PDB code: 8BZ7; chain A) and RmlT$_{D198A}$ (grey, PDB code: 8BZ8; chain F) in
252 complex with TDP-rhamnose through Cα of residues 110, 112-113 and 197-198 (Cα RMSD: 0.245 Å). Apparent change
253 in the position of rhamnose moiety is indicated by arrow. **c)** Impact of mutations in the active site of RmlT on *L.*
254 *monocytogenes* surface rhamnosylation. Fluorescence microscopy analysis of *L. monocytogenes* strains EGDe wild-type,
255 EGDe Δ*rmlT* and EGDe Δ*rmlT* complemented with *rmlT*, *rmlT$_{W89A}$*, *rmlT$_{E197A}$*, *rmlT$_{D198A}$* or *rmlT$_{W223A}$*. Bacterial cells
256 and the rhamnose at the bacterial surface were stained with wheat germ agglutinin (WGA, red) and gp17-GFP rhamnose
257 binding protein (green), respectively. **d)** Quantification of the fluorescence associated to gp17-GFP bound to rhamnose
258 at the surface of the strains in c). Mean ± SD (n = 3) and individual measurements are shown; one-way ANOVA; ** $p <$
259 0.01, *** $p < 0.001$, **** $p < 0.0001$.

260

261 **RmlT specificity for TDP-rhamnose is not determined by ligand affinity**

262 The lack of strong contacts between rhamnose and RmlT residues raised the possibility that the
263 enzyme is not selective relative to the donor substrate sugar. To explore this hypothesis, we measured
264 RmlT activity using the free-phosphate coupled functional assay in the presence of naked WTAs and
265 the nucleotides TDP-rhamnose, TDP-glucose, UDP-glucose and UDP-GlcNAc as well as L-
266 rhamnose. The amount of phosphate detected was higher with TDP-rhamnose relative to all other
267 donor substrates tested, demonstrating a catalytic preference of RmlT for this nucleotide (Figure 5A).

268 To evaluate in more detail the molecular basis of RmlT specificity, we used isothermal titration
269 calorimetry (ITC) to determine its affinity for different donor substrates in the absence of WTAs
270 (Figure 5B). TDP-rhamnose bound to RmlT with a K_D of ~13 μM, with 1 molecule bound per RmlT
271 subunit. Surprisingly, TDP-glucose bound RmlT as well as TDP-rhamnose (K_D = ~10 μM).
272 Moreover, TDP also bound RmlT with a slightly lower affinity (K_D = ~50 μM). We could not detect
273 binding of UDP-glucose in the experimental conditions used. These results indicate that the
274 nucleotide moiety (TDP) determines most of the strength of the interaction between the donor
275 substrate and RmlT.

276 Using a high concentration (5 mM) of UDP-glucose, we determined the structure of its complex with
277 RmlT (PDB code: 8BZ6) at 2.4 Å (Figure 5C, Table 1 and supplementary Table 1). The structure
278 reveals few changes relative to RmlT/TDP-rhamnose and does not provide obvious hints for the
279 preference towards TDP. The two nucleotides, TDP and UDP, differ in two chemical groups, a
280 methyl group in the thymidine and a hydroxyl group in the ribose of UDP (Figure 5D). The methyl
281 group in the base is within Van der Waals distance of Y28 but generally points away from the protein,
282 while the extra hydroxyl in UDP is within hydrogen bonding distance of P26 main-chain carbonyl
283 and appears to be accommodated with very slight changes in the protein. We also searched for clues
284 that could explain a preference for rhamnose over glucose. Interestingly, the position and
285 conformation of the sugar in UDP-glucose is significantly better defined than that of the rhamnose
286 in the TDP-rhamnose structures (Supplementary Figures 3E-F, 5C and 9). This could reflect that the
287 glucose is better stabilized in the sugar binding pocket resulting in reduced ability to acquire the
288 proper position for catalysis when the acceptor WTAs is present. Moreover, while the glucose moiety
289 in UDP-glucose establishes hydrogen bonds with E197 (Figure 5C), rhamnose in TDP-rhamnose is
290 hydrogen bound to D198 (as discussed above).

291 Altogether, our results show that selection of the donor nucleotide does not result from interactions
292 between the sugar and RmlT, but is determined in the ternary complex.

293 To gain insights into the donor substrate selectivity mechanism, we mixed RmlT with naked WTAs
294 in the presence of the same concentrations of either TDP-rhamnose, TDP-glucose or UDP-glucose,
295 and quantified RmlT activity by measuring released phosphate over time. As before, activity detected
296 with TDP-rhamnose was much higher than with the other nucleotides (Figure 5E). We then measured
297 RmlT activity in a competition experiment where the reaction contained equal amounts of TDP-
298 rhamnose and TDP-glucose. If donor specificity is thermodynamically determined in the ternary
299 complex, then the rate of the reaction should not change much with the addition of TDP-glucose
300 since most of the ternary complexes will contain TDP-rhamnose. However, if the two donor
301 nucleotides bind equally well and specificity is determined by another mechanism, we should observe
302 a clear reduction in the rate of reaction, since only the fraction of the ternary complexes with bound
303 TDP-rhamnose will result in sugar transfer. The time course of the TDP-rhamnose/TDP-glucose
304 mixture showed a clear decrease in the initial activity rate calculated from the first 2 minutes, from
305 4.8 to 1.4 μM phosphate released/min/μM RmlT (Figure 5E). Moreover, when RmlT was incubated
306 with mixed TDP-rhamnose and UDP-glucose (which binds very weakly to RmlT), the reaction
307 occurred as in the presence of only TDP-rhamnose. In summary, these results support the proposal
308 that RmlT specificity is not determined by the affinity of the donor substrate. Instead, the presence
309 of rhamnose in the catalytic site increases either the binding affinity of WTAs or the efficiency of
310 sugar transfer.
311

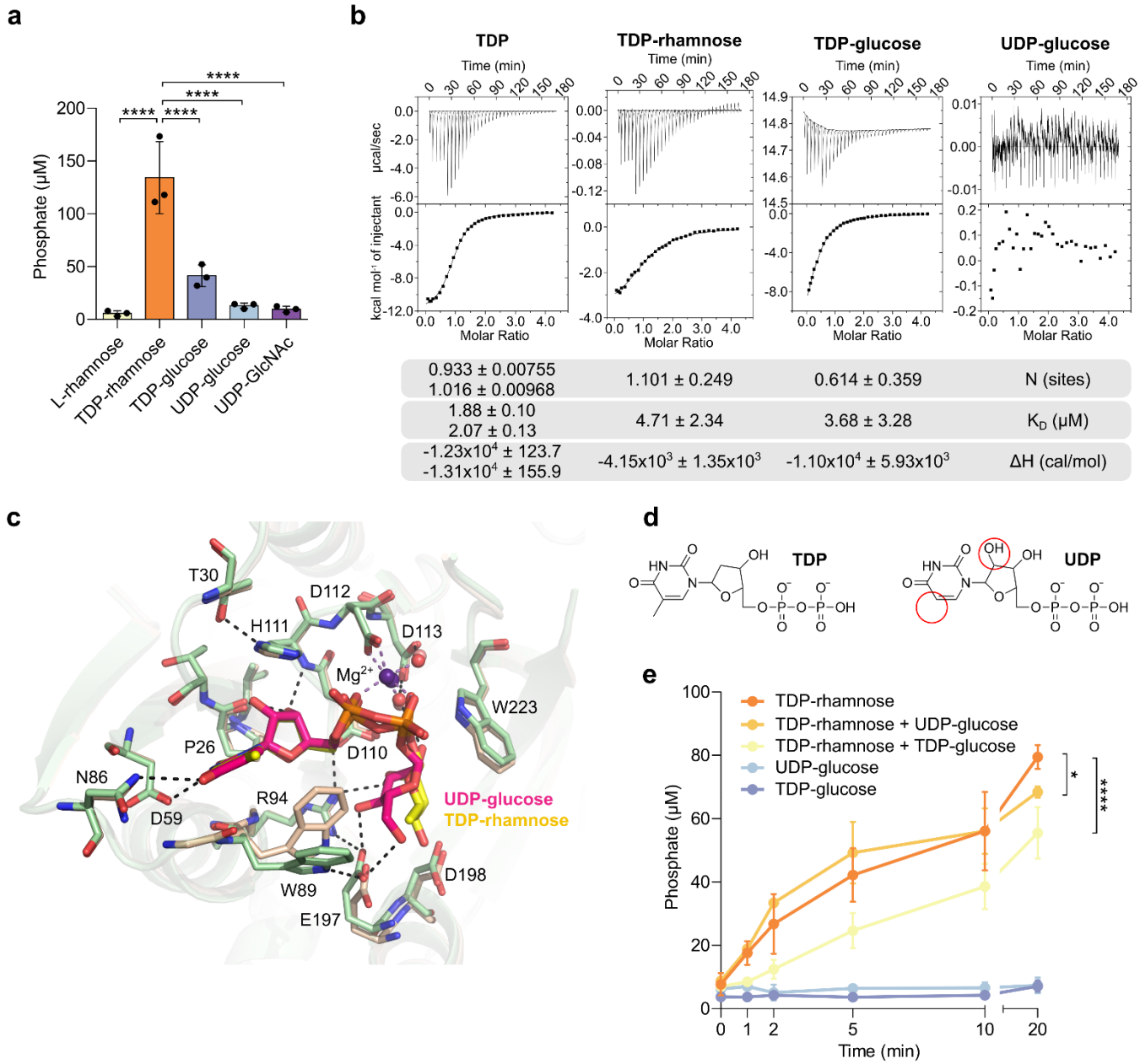

Figure 5: Donor substrate selectivity in RmlT. **a)** Purified recombinant RmlT (2 µM) was incubated with 1mM WTAs and 200 µM TDP-rhamnose, L-rhamnose, TDP-glucose, UDP-glucose or UDP-GlcNAc. RmlT activity was measured after 30 minutes by quantifying released phosphate. **b)** ITC measurement of RmlT/donor substrate interactions. Upper panels show the titration of RmlT with TDP-rhamnose, TDP-glucose, TDP or UDP-glucose. The lower panel shows heat released when substrate binds to RmlT as a function of relative concentrations. Dilution heat was corrected. Solid lines correspond to the best fit of data using a bimolecular interaction model. Table shows N-value (commonly referred as the stoichiometry), binding constant K_D (µM) and reaction enthalpy (ΔH) extracted from model fitting. **c)** Superposition of active-sites of RmlT/UDP-glucose (green with UDP-glucose in pink, PDB code: 8BZ6; chain D) and RmlT/TDP-rhamnose (wheat with TDP-rhamnose in yellow, PDB code: 8BZ7; chain D) through residues 467-477 (Cα RMSD: 0.114 Å) with the substrate-interacting residues shown as sticks. Hydrogen bonds between RmlT residues and UDP-glucose are represented as black dashed lines. Water and Mg^{2+} are shown as red and purple spheres, respectively. **d)** Chemical structure of TDP (left) and UDP (right) with differences highlighted by red circles. **e)** Quantification of phosphate

325 released over time for RmlT incubated with different donor substrates. Reactions contained 1 mM WTAs, 200 µM of
326 each nucleotide and 2 µM RmlT. Mean ± SD (n = 3, except for the curve of TDP-glucose in which n = 4) are shown for
327 a) and e); individual values shown in a); two-way ANOVA; * $p < 0.05$, **** $p < 0.0001$.

328

329 **RmlT rhamnosylates naked WTAs**

330 We also wondered if RmlT displays specificity towards WTAs modifications, in particular WTAs
331 glycosylations. We thus analysed RmlT activity in the presence of TDP-rhamnose and WTAs
332 purified from wild-type EGDe strain and isogenic mutants presenting different glycosylation
333 patterns: decorated with rhamnose at position *C*-4 and GlcNAc at *C*-2 of the ribitol-phosphate (RboP)
334 units (isolated from wild-type *L. monocytogenes* EGDe strain), decorated only with GlcNAc (from
335 the EGDe Δ*rmlT* strain), decorated only with rhamnose (from the EGDe Δ*lmo1079* strain), or without
336 any decoration (naked WTAs) isolated from the EGDe Δ*rmlTΔlmo1079* strain. While some RmlT
337 activity was detected with rhamnose-decorated WTAs, suggesting incomplete glycosylation at *C*-4,
338 the strongest activity of RmlT was detected in the presence of naked WTAs (Figure 6A). Importantly,
339 no activity was observed with WTAs containing only GlcNAc, indicating that the presence of
340 GlcNAc impairs RmlT activity and strongly suggesting that in the bacterial cell, RmlT likely
341 functions before the glycosyltransferase (Lmo1079) that adds GlcNAc on WTAs.

342 To better understand the molecular characteristics of the complex formed by RmlT and WTAs, we
343 determined the structure of RmlT with two different synthetic WTAs, with 3 or 4 RboP units (Figure
344 6B), at 2.34 (PDB code: 9GZJ) and 2.52 Å (PDB code: 9GZK), respectively (Table 1 and
345 supplementary Table 1). We also attempted to obtain diffracting crystals of the ternary complexes of
346 RmlT with synthetic WTAs and either TDP-rhamnose or TDP-glucose, but diffraction quality was
347 very poor (10 Å or worse). The RmlT/WTAs structures are globally similar to the apo-structure, with
348 both structures showing detailed electron-density in all copies for 2 units of RboP in the vicinity of
349 the catalytic residue D198 (binding site 1) (Figure 6C, Supplementary Figures 10 and 11).
350 Interactions formed by the RboP units with the protein are detailed in Figure 6C. In particular, the
351 phosphate group from the RboP in the subsite closest to the catalytic residues (subsite +1) interacts
352 directly with side-chains of H268 and R273 (residues conserved in TarS, H253 and R258) and
353 indirectly with W269 through a water molecule, as well as with the main-chain amino group of M170.
354 In addition, the catalytic residue D198 is within hydrogen bond distance (2.8 and 2.9 Å) of the
355 hydroxyls in *C*-3 and *C*-4, appearing to orient the *C*-4 hydroxyl group for nucleophilic attack on the
356 sugar anomeric carbon in the donor substrate, as observed in a superposition of the binary complex
357 structures with TDP-rhamnose and WTAs (Figure 6D). In addition, the RboP in subsite +2 (further

358 from the catalytic site) establishes interactions through the phosphate group with S146, W149 and
359 R474, through the hydroxyl in *C*-2 with the main-chain amino group of G148 and through Van der
360 Walls contacts of *C*-1 and *C*-2 with the face of W147. Importantly, the WTAs structures provide an
361 explanation for why RmlT prefers naked WTAs and cannot rhamnosylate WTAs modified with
362 GlcNAc at *C*-2 since there is relatively little space around the hydroxyl at position *C*-2 in subsites +1
363 and +2 (Figure 6C).

364 Analysis of several structures provides clues for two possible interaction pathways taken by longer
365 WTAs bound to RmlT. In the RmlT/WTAs structures, electron-density compatible with a second
366 molecule of synthetic WTAs is present in some RmlT copies on the oligomerization domain (Figure
367 6C, Supplementary Figures 10 and 11). The lack of this density in other copies in the asymmetric
368 unit seems linked to the formation of a crystal contact. We built a short WTAs into this density.
369 Additionally, in the high resolution apo-RmlT structure (PDB code 8BZ5), HEPES molecules are
370 present at different sites on the positively charged surface of the protein, with their sulphate groups
371 nicely superposing with either the phosphate groups of RboP in binding sites 1 and 2 or with a strong
372 electron-density observed in the RmlT/WTAs complex (not modelled) in binding site 3
373 (Supplementary Figure 12).

374 Altogether, this evidence suggests that, in binding pathway 1, long WTAs snakes through the
375 oligomerization domain from binding site 2 into binding site 1, which is placed in a deep cleft close
376 to the catalytic site (Figure 6E, Supplementary Figure 12).

377 However, a comparison of the RmlT/WTAs complex structures with the structures of TarP bound to
378 similar synthetic WTAs (PDB codes: 6H4M, 6HNQ and 6H4F) (Figure 6E) suggests an alternative
379 pathway. The comparison shows the WTAs sitting in equivalent clefts (corresponding to binding site
380 1) in the two structures (Figure 6E). The WTAs in the TarP structure have an extra RboP unit,
381 corresponding to subsite +3, which in RmlT is positioned inside the tunnel formed by the catalytic,
382 helical and oligomerization domains. This observation suggests that, in binding pathway 2, the long
383 WTAs snakes through the tunnel into binding site 1, towards the catalytic site.

384 Binding pathway 2 raises the question of how would a long WTAs enter the tunnel. The strong
385 structural similarity between RmlT and TarS (Supplementary Figure 1) [27] leads to the hypothesis
386 that, like in TarS, the oligomerization domain of RmlT can adopt different positions relative to the
387 catalytic domain so that there is a closed conformation, corresponding to the crystallographic
388 structure, and an open conformation that allows access of the WTAs polymer to its binding groove
389 and the tunnel. To explore this hypothesis, we generated a metal bridge across the

390 catalytic/oligomerization interface by mutating two residues that are in close proximity to cysteine
391 (W145 on the catalytic subdomain and A472 on the oligomerization subdomain) (Figure 6E) and
392 performed the rhamnosylation reaction in the absence and presence of cadmium. Cadmium
393 coordination by the two cysteines will bridge the two subdomains and stabilize the interface [31]. If
394 a transition between the closed and open conformations is important for the rhamnosylation reaction
395 of WTAs, then formation of the metal bridge will reduce activity. The mutant protein functioned as
396 well as wild-type RmlT in the absence of cadmium cation, and the addition of 100 μM of $CdCl_2$ had
397 no impact the activity of wild-type RmlT. However, Cd^{2+} reduced the activity of the mutant protein
398 by more than 50% (Figure 6F), supporting the proposal of the existence of an open conformation in
399 the catalytic mechanism of RmlT and supporting WTAs binding pathway 2 as a viable option that
400 merits future exploration.

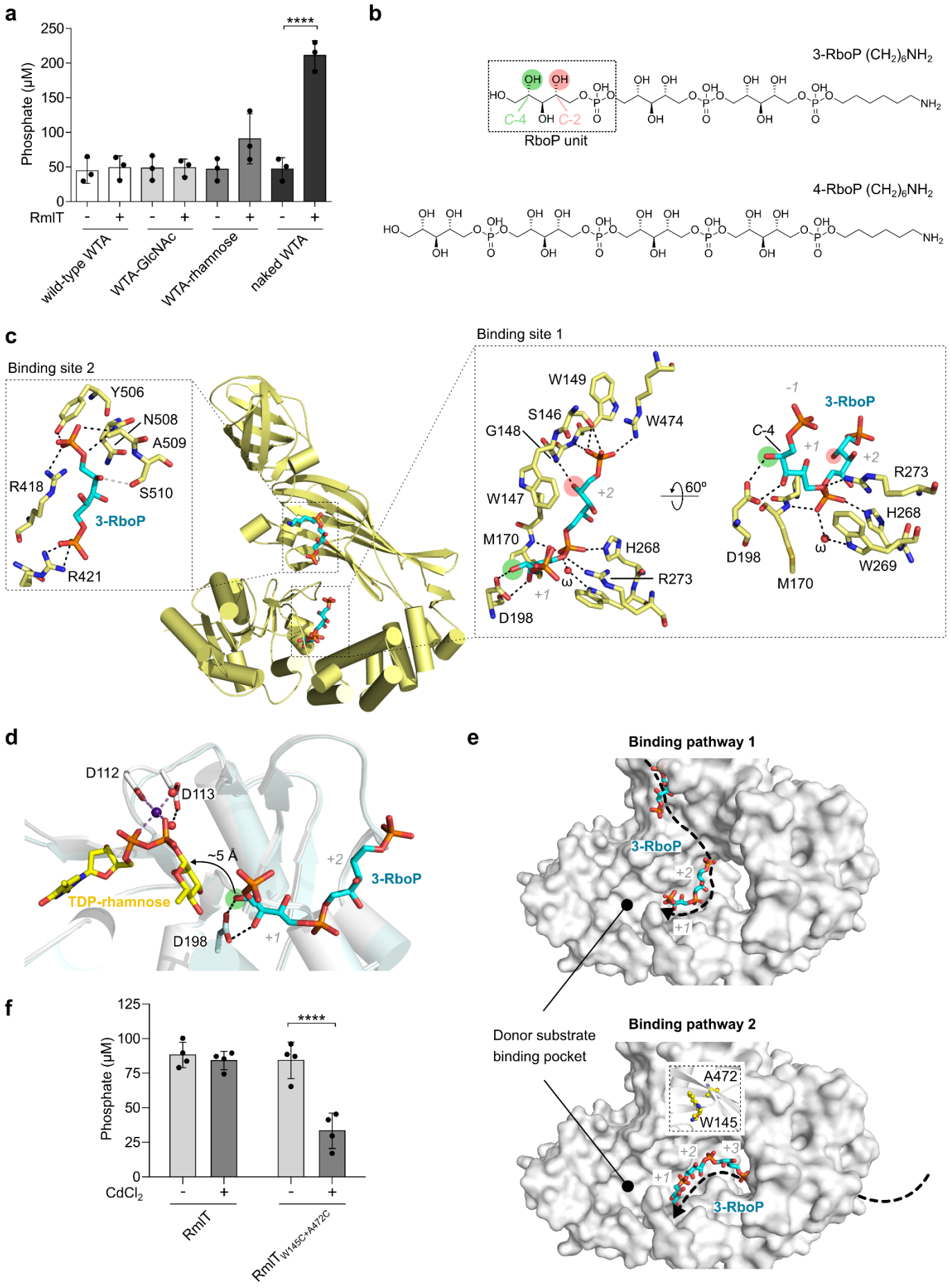
a
Phosphate (μM)
250
200
150
100
50
0
****
RmlT
-
+
-
+
-
+
-
+
wild-type WTA
WTA-GlcNAc
WTA-rhamnose
naked WTA
b
3-RboP (CH2)6NH2
C-4
C-2
RboP unit
4-RboP (CH2)6NH2
c
Binding site 2
Y506
N508
A509
R418
S510
3-RboP
R421
Binding site 1
W149
S146
W474
G148
W147
+2
60°
M170
H268
R273
ω
+1
D198
-1
3-RboP
C-4
+1
+2
R273
H268
D198
ω
W269
M170
d
D112
D113
~5 Å
+2
3-RboP
TDP-rhamnose
D198
+1
e
Binding pathway 1
3-RboP
+2
+1
Donor substrate
binding pathway
Binding pathway 2
A472
W145
+2
+3
+1
3-RboP
f
Phosphate (μM)
125
100
75
50
25
0
****
CdCl2
-
+
-
+
RmlT
RmlTW145C+A472C

402 **Figure 6**: Structure of RmlT with bound poly-ribitol phosphate. **a)** Quantification of phosphate released from TDP
403 generated by RmlT in presence of differently decorated WTAs: containing both GlcNAc and rhamnose modifications
404 (wild-type WTAs), only GlcNAc modification (WTAs-GlcNAc), only rhamnose modification (WTAs-rhamnose) or
405 without any glycosylation (naked WTAs). Reaction mixtures included 5 mM WTAs, 1 mM TDP-rhamnose and 10 µM
406 RmlT incubated during 30 minutes. Mean ± SD (n = 3) and individual measurements are shown; one-way ANOVA, ****
407 = $p < 0.0001$. **b)** Chemical structures of 3-RboP and 4-RboP with ribitol-phosphate unit indicated together with *C*-2 (light
408 red) and *C*-4 (light green). **c)** Cartoon representation of RmlT with two bound RboP chains represented as sticks (PDB
409 code 9GZJ chain A). Molecular details of RboP binding sites are shown, with subsites occupied by separate RboP units
410 numbered +1 and +2. Atoms within hydrogen bond distance indicated by dashed lines. *C*-4 hydroxyl in subsite +1 is
411 highlighted by green circle; *C*-2 hydroxyl in subsite +2 is highlighted by red circle. **d)** Comparison of active-sites in
412 RmlT/TDP-rhamnose (white with TDP-rhamnose in yellow; PDB code 8BZ7 chain D) and RmlT/3-RboP (light cyan
413 with 3-RboP in cyan; PDB code 9GZJ chain A). Structures are shown in same view after superposition through Cα atom
414 of resides 238-516 (RMSD=0.364 Å). TDP/rhamnose, 3-RboP, residues D112 and D113 and D198 are shown as sticks.
415 Mg^{2+} and water molecules are represented by purple and red spheres. Dashed lines indicate atoms within hydrogen bond
416 or coordinating the metal. **e)** TarP/6RboP-(CH2)6NH2 (top image; PDB code 6HNQ chain A) and RmlT/3-RboP
417 (bottom; PDB code 9GZJ chain A) in the same orientation (superposed through Cα atom pairs of RmlT residues 93-100
418 and 198-204 and TarP residues 75-82 and 181-187 (RMSD 0.672 Å)). Subsites are indicated (+1, +2 and +3). **f)**
419 Quantification of phosphate released from TDP generated by RmlT or $RmlT_{W145C+A472C}$ incubated with naked WTAs and
420 TDP-rhamnose for 30 minutes in the presence or absence of 100 µM of $CdCl_2$. Mean ± SD (n = 4) and individual
421 measurement are shown; two-way ANOVA; **** $p < 0.0001$.
422

423 **RmlT is a potential target for anti-virulence approaches**

424 Previously, we demonstrated that deletion of the gene coding for RmlT in *L. monocytogenes* EGDe
425 results in virulence attenuation in mouse spleens and livers, and that this virulence defect is reverted
426 to wild-type levels by complementation with the wild-type RmlT (EGDe Δ*rmlT::rmlT*) [13, 14, 16,
427 17]. To further demonstrate the direct importance of the catalytic activity of RmlT for the virulence
428 of *L. monocytogenes*, we assessed in the same mouse infection model the virulence of the *L.*
429 *monocytogenes* EGDe Δ*rmlT* strain complemented with the catalytic-deficient $RmlT_{D198A}$ mutant
430 (EGDe Δ$rmlT::rmlT_{D198A}$) and compared it with the Δ*rmlT* strain complemented with the wild type
431 RmlT. We first demonstrated that similar protein levels of RmlT and $RmlT_{D198A}$ are produced by
432 wild-type *L. monocytogenes* EGDe and complemented EGDe Δ*rmlT* strains (Supplementary Figure
433 14). Mice were then intravenously infected with *L. monocytogenes* EGDe Δ*rmlT*, Δ*rmlT::rmlT* or
434 Δ$rmlT::rmlT_{D198A}$, and bacterial load per spleen and liver was assessed 72 h post-infection (Figure
435 7). Compared to the number of bacteria present in organs of animals infected with the *L.*
436 *monocytogenes* EGDe Δ*rmlT* strain, the complementation with wild-type RmlT (EGDe
437 Δ*rmlT::rmlT*) induced a significant increase in the number of bacteria present in both organs,
438 restoring full bacterial virulence as previously observed [13]. In contrast, complementation with the

439 inactive RmlT variant (EGDe Δ*rmlT::rmlT*$_{D198A}$) did not increase the number of bacteria present in
440 the organs of infected mice. These results indicate that inactivation of RmlT by a single mutation in
441 its active site generates attenuated bacteria, serving as a proof of concept to demonstrate the potential
442 of the inhibition of the catalytic activity of RmlT as a new anti-virulence approach.

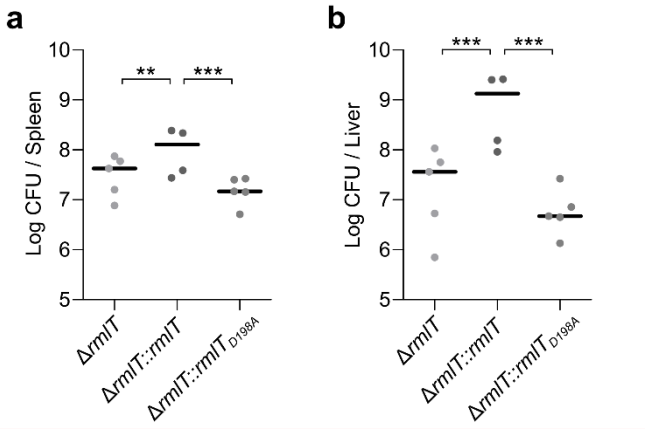

443

444 **Figure 7**: Impact of RmlT activity in the ability of *L. monocytogenes* to infect mice. Bacterial counts in the spleens (**a**)
445 and livers (**b**) of the mice 72h after intravenous inoculation of the *L. monocytogenes* strains EGDe Δ*rmlT*, EGDe
446 Δ*rmlT*::*rmlT* or EGDe Δ*rmlT*::*rmlT*$_{D198A}$. Data are presented as scatter plots, with the counts for each animal indicated
447 by dots and the mean by a horizontal line (n = 5, except for EGDe Δ*rmlT*::*rmlT* in which n = 4); one-way ANOVA; ** p
448 < 0.01, *** p < 0.001.

449

450 **Discussion**

451 Glycosylation of WTAs from Gram-positive pathogens is crucial for bacterial virulence and
452 resistance to antimicrobials. Despite the significant impact of WTAs glycosyltransferases on crucial
453 aspects of bacterial infection, identification and characterization of these enzymes, which represent
454 promising targets for novel anti-virulence strategies, has been limited. In this study, we have
455 elucidated the first structure and uncovered functional details of a bacterial WTAs
456 rhamnosyltransferase, RmlT, expressed by the major Gram-positive foodborne pathogen *L.*
457 *monocytogenes*. Structural analysis of RmlT reveals strong similarities with the structure of *S. aureus*
458 glycosyltransferase TarS [27], both sharing the same tertiary organization in the catalytic, helical,
459 oligomerization and turret subdomains. The catalytic and helical subdomains of these proteins are
460 also identical in a third glycosyltransferase, *S. aureus* TarP [24]. In addition, many of the residues
461 present in the active site of RmlT are conserved in TarS and TarP [24, 27]. The most striking
462 difference is that RmlT assembles as a dimer while TarS and TarP form trimers [24, 27]. We showed
463 that the dimer interface is important for the physiological function of RmlT since mutations on the

464 interface designed to disrupt the dimer architecture retained catalytic activity but altered the
465 rhamnosylation pattern of the bacterial surface *in vivo*.
466 Although we have previously demonstrated that in *L. monocytogenes* the gene coding for RmlT is
467 required for the decoration of WTAs with rhamnose [13], the activity of the enzyme had never been
468 characterized. We now have shown, using two different assays, that RmlT in the presence of TDP-
469 rhamnose and naked WTAs alters the electrophoretic mobility of WTAs in a native-PAGE and
470 releases TDP, consistent with the transfer of rhamnose from the donor substrate to WTAs. Given the
471 high conservation of the catalytic residues across different WTAs glycosyltransferases, we wondered
472 what drives the specificity of RmlT activity for TDP-rhamnose. Using a combination of approaches,
473 we showed that RmlT binds equally well to TDP-rhamnose and TDP-glucose but only transfers
474 rhamnose to WTAs, suggesting that specificity is either kinetically determined or depends on a
475 cooperative binding effect between the WTAs and the correct donor substrate. Similar results were
476 reported for *B. subtilis* TagA, a teichoic acid glycosyltransferase. TagA binds both UDP-*N*-
477 acetylmannosamine (UDP-ManNAc) and UDP-GlcNAc but is enzymatically active only with UDP-
478 ManNAc [32]. This finding raises the question of how the efficiency of WTAs rhamnosylation is
479 ensured in bacteria since other TDP coupled sugars will compete for the TDP-rhamnose binding site,
480 slowing the production of decorated WTAs.

481 Our structures provide a clarification for the role of the catalytic residue D198, which aligns with the
482 proposed catalytic residue in *S. aureus* Tar proteins [24, 27]. In the binary complex with the acceptor
483 substrate, D198 forms hydrogen bonds with *C*-3 and *C*-4 of the ribitol-phosphate at the catalytic site,
484 suggesting that D198 catalyses the reaction by orienting the hydroxyl towards the anomeric carbon
485 of the sugar and by acting as a base that promotes the nucleophilic character of the hydroxyl group.

486 In addition, we showed that RmlT displays specificity for WTAs, glycosylating naked WTAs that
487 lacks both rhamnose and GlcNAc. The binary complex structure with synthetic WTAs reveals that
488 this RmlT preference results from steric hindrance at *C*-2 substitutions.

489 Overall, our data provides a novel insight into the molecular mechanism of WTAs
490 glycosyltransferases. The RmlT structure in complex with WTAs offers clues about the long WTAs
491 pathway on the protein surface. In particular, a second RboP binding site suggests that the polymer
492 runs along the oligomerization domain into the deep cleft that leads to the catalytic site. Alternatively,
493 comparison between the structures of RmlT and TarP and biochemical crosslinking across the
494 interface between the RmlT catalytic and oligomerization subdomains, suggests that RmlT undergoes
495 a transition between an open conformation, where the catalytic-oligomerization interface is not
496 established and the WTAs polymer can bind to the protein, and a closed conformation, where the

497 interface is formed and the polymer is trapped inside the tunnel formed by the catalytic,
498 oligomerization and helical subdomains. In this alternative pathway, long WTAs run through the
499 tunnel towards the catalytic site. Further studies are required to distinguish between these two
500 possibilities and their impact on the lifetime of the enzyme-WTAs complex and on the potential
501 processivity of the enzyme as proposed for TarS and TarP (Figure 8) [24, 27].

502 By combining our findings with earlier discoveries, we clarified several stages of WTAs
503 glycosylation in *L. monocytogenes* serovar 1/2a. In particular, our data supports that the newly
504 formed WTAs is first decorated with rhamnose by RmlT. This indicates that decoration with GlcNAc
505 by Lmo1079 follows rhamnosylation, fitting well with the physiological location of RmlT in the
506 cytosol and of Lm1079 on the external surface of the plasma membrane (Figure 8). We also suggest
507 that rhamnosylation (step 1) involves a close interaction of RmlT with a long stretch of ribitol-
508 phosphate units in the WTAs, favouring multiple cycles of rhamnosylation before release of the
509 decorated WTAs. Flipping of the rhamnosylated WTAs to the outside of the cell membrane (step 2)
510 is likely to result from the action of a homolog of the *S. aureus* TarGH ABC transporter (predicted
511 to be Lmo1074-75) [35, 36]. In parallel, it has been proposed that the cytoplasmic glycosyltransferase
512 Lmo2550 uses UDP-GlcNAc to form a C_{55}-P-GlcNAc WTAs intermediate that is also flipped across
513 the membrane by the flippase GtcA [29]. The membrane-associated glycosyltransferase Lmo1079
514 then transfers the GlcNAc moiety to the rhamnosylated-WTAs backbone on the outside of the cell
515 [37, 38] (step 3). Finally, the mature WTAs is transferred to the bacterial cell wall by a still unclear
516 mechanism proposed to be promoted in *S. aureus* by the TarTUV enzymes (step 4) [33].
517

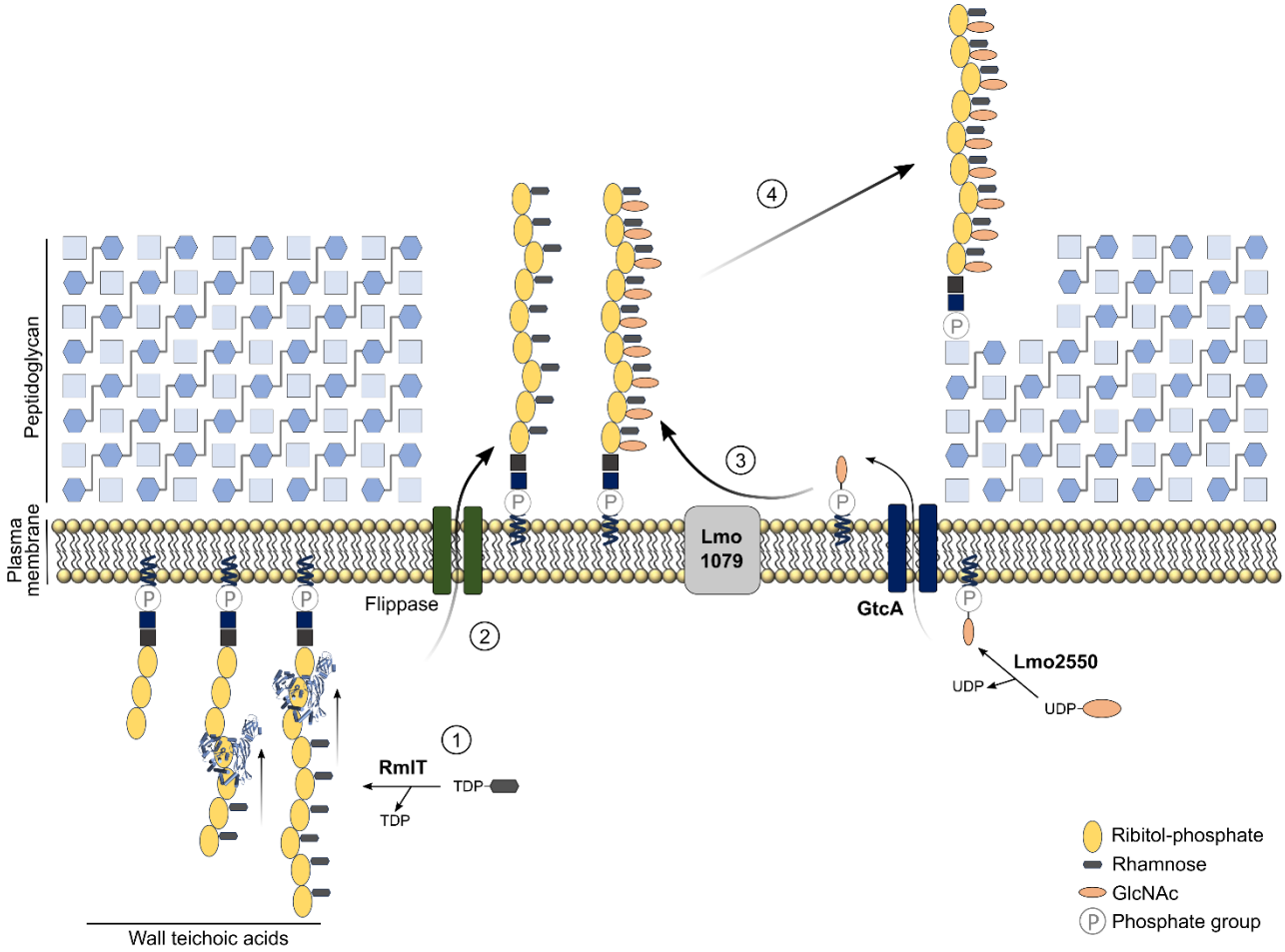

Figure 8: Proposed model for the glycosylation of WTAs in *L. monocytogenes* EGDe serovar 1/2a. Step 1: In the cytoplasm, RmlT decorates newly formed chains of ribitol-phosphate with rhamnose units from TDP-rhamnose. Step 2: Rhamnosylated WTAs are flipped across the membrane, probably by the Lmo1074-75 complex, homolog to the *S. aureus* two-component ATP-binding cassette (ABC) transporter TarGH. Step 3: Rhamnosylated WTAs are glycosylated by Lmo1079 with GlcNAc from a C_{55}-P-GlcNAc intermediate previously formed by the cytoplasmic glycosyltransferase Lmo2550 using UDP-GlcNAc and then flipped across the membrane by the GtcA flippase. Step 4: Fully decorated WTAs are anchored to the cell wall, possibly by a homolog of the *S. aureus* TarTUV complex.

In summary, WTAs glycosylations are involved in many bacterial features across different species including bacterial virulence [13, 14], resistance to antibiotics [16, 23, 25, 39-42] and antimicrobial peptides [13] and in the localization of important surface proteins that facilitate host immune evasion and colonization [23, 25, 39, 40]. Therefore, it is tempting to consider glycosylation of bacterial WTAs as a conserved virulence mechanism in Gram-positive pathogens. Importantly, our experiments proved that mutation of a single residue in the active site of RmlT leads to enzyme inactivation and to a significant decrease in the capacity of *L. monocytogenes* cells to infect mice. Together with the relatively weak binding selectivity for TDP-modified molecules, this indicates that

536 RmlT is a valid target for the development of next-generation antibacterial drugs that, by inhibiting
537 specific sugar decorations, will not directly kill bacteria but will diminish bacterial virulence, increase
538 susceptibility to host innate defences and potentiate the action of antibiotics while preserving the
539 microbiota.
540

541 **Methods**

542

543 **Cloning**

544 *rmlT* was cloned into the expression vector pET28b by the polymerase incomplete primer
545 extension method [43]. Briefly, *rmlT* was amplified by PCR from the *L. monocytogenes* EGDe
546 (ATCC-BAA-679) genomic DNA, using primers #1 and #2. Vector pET28b was amplified by
547 PCR using primers #3 and #4. Both reactions generated a mixture of incomplete extensions
548 products that contained short overlapping sequences at the ends, allowing the annealing of the
549 complementary strands to produce hybrid vector-insert combinations. Vectors and primer
550 sequences are presented in Supplementary Table 2 and 3, respectively.

551

552 **Site-directed mutagenesis**

553 Vectors pET28b-*rmlT*$_{D198A}$, pET28b-*rmlT*$_{D197A}$, pET28b-*rmlT*$_{W89A}$, pET28b-*rmlT*$_{W223A}$,
554 pET28b-*rmlT*$_{Y368A+E372A}$, pET28b-*rmlT*$_{Y347A+Y368A+E372A}$, pET28b-*rmlT*$_{W145C+A472C}$, pPL2-
555 *rmlT*$_{D198A}$, pPL2-*rmlT*$_{D197A}$, pPL2-*rmlT*$_{W89A}$, pPL2-*rmlT*$_{W223A}$, pPL2-*rmlT*$_{Y368A+E372A}$ and
556 pPL2-*rmlT*$_{Y347A+Y368A+E372A}$ were obtained by site-directed mutations using pET28b-*rmlT* or
557 pPL2-*rmlT* [13] as templates and primer pairs #5 and #6 (for pET28b-*rmlT*$_{D198A}$ and pPL2-
558 *rmlT*$_{D198A}$), #7 and #8 (for pET28b-*rmlT*$_{D197A}$ and pPL2-*rmlT*$_{D197A}$), #9 and #10 (for pET28b-
559 *rmlT*$_{W89A}$ and pPL2-*rmlT*$_{W89A}$), #11 and #12 (for pET28b-*rmlT*$_{W223A}$ and pPL2-*rmlT*$_{W223A}$), #13
560 and #14 (for pET28b-*rmlT*$_{Y368A+E372A}$ and pPL2-*rmlT*$_{Y368A+E372A}$), #13, #14 #15 and #16 (for
561 pET28b-*rmlT*$_{Y347A+Y368A+E372A}$ and pPL2-*rmlT*$_{Y347A+Y368A+E372A}$) and #17, #18, #19, #20 (for
562 pET28b-*rmlT*$_{W145C+A472C}$). Primer information is presented in Supplementary Table 3.
563 Mutations were confirmed by sequencing.

564

565 **Synthesis of 3RboP and 4RboP**

566 3RboP and 4RboP were synthesized as previously described [39, 44].

567

568 **Expression and purification of RmlT variants**

569 *Escherichia coli* BL21(DE3) cells transformed with pET28b encoding N-terminally
570 hexahistidine tagged RmlT (pET28b-*rmlT*), RmlT$_{D198A}$ (pET28b-*rmlT*$_{D198A}$), RmlT$_{D197A}$
571 (pET28b-*rmlT*$_{D197A}$), RmlT$_{W89A}$ (pET28b-*rmlT*$_{W89A}$), RmlT$_{W223A}$ (pET28b-*rmlT*$_{W223A}$),
572 RmlT$_{Y368A+E372A}$ (pET28b-*rmlT* $_{Y368A+E372A}$), RmlT$_{Y347A+Y368A+E372A}$ (pET28b-*rmlT*
573 $_{Y347A+Y368A+E372A}$) or RmlT$_{W145C+A472C}$ (pET28b-*rmlT* $_{W145C+A472C}$) were grown in LB
574 supplemented with 30 μg ml^{-1} kanamycin at 37°C for 3 h. Protein expression was induced with

575 0.5 mM isopropyl β-D-1-thiogalactopyranoside (IPTG). After 16 h-growth at 30°C, cells were
576 harvested, resuspended in lysis buffer (50 mM NaH_2PO_4 pH 8.0, 300 mM NaCl, 10 mM
577 Imidazole) and lysed by sonication. Cell lysate was clarified by centrifugation and incubated
578 with an immobilized metal-affinity matrix (Ni-NTA Agarose, ABT Technologies), pre-
579 equilibrated with lysis buffer, at 4°C for 1 h. After washing the beads with 50 mM NaH_2PO_4
580 pH 8.0, 300 mM NaCl, 30-50 mM Imidazole, proteins were eluted with 50 mM NaH_2PO_4, 300
581 mM NaCl, pH 8.0, 100-300 mM Imidazole. Eluted material was concentrated using a 30 kDa
582 cut-off membrane concentrator (Vivaspin, Sartorius Stedim Biotech) concomitantly with
583 buffer exchange to 20 mM Tris-HCl pH 8.0, 100 mM NaCl, 1 mM DTT. Hexahistidine tag
584 (His-tag) was removed by digestion with TEV protease (1:10 molar ratio) at 4°C for 16 h.
585 Proteins were separated from TEV protease, His-tag and uncut proteins by a second
586 immobilized metal-affinity column pre-equilibrated with storage buffer (20 mM Tris-HCl pH
587 8.0, 100 mM NaCl, 1 mM DTT). Flow-through containing untagged protein was concentrated
588 and loaded into a Superdex-200 10/300 GL column (GE Healthcare) pre-equilibrated with
589 storage buffer. Fractions containing pure protein were pooled and concentrated. Protein
590 concentration was estimated by measuring absorbance at 280 nm and using extinction
591 coefficients calculated with the ExPASY tool Protparam. Purified RmlT variants were flash-
592 frozen in liquid nitrogen and stored at -80 °C.
593
594 **Expression and purification of selenomethionine-containing RmlT variant**
595 *E. coli* B834(DE3) cells transformed with pET28b-*rmlT* were grown in 20 mL LB medium
596 overnight at 37°C. Cells were collected, washed three times with sterile deionized water and
597 inoculated into selenomethionine medium (Molecular Dimensions). Protein expression and
598 purification was performed as described above.
599
600 **Crystallization of RmlT variants**
601 Initial crystallization conditions for RmlT were determined at 20°C using commercial sparse-
602 matrix crystallization screens. Sitting-drop vapor diffusion experiments were set up in 96-well
603 CrystalQuick plates using an Oryx 4 crystallization robot (Douglas Instruments). Drops
604 consisted of equal volumes (0.3 µL) of RmlT protein solution (at 10 mg mL^{-1} in 20 mM Tris-
605 HCl pH 8.0, 100 mM NaCl, 1 mM DTT) and crystallization solution, equilibrated against 40
606 µL reservoir solution. The apo RmlT structure with bound HEPES was obtained from a crystal
607 grown in solution B9 from JBScreen Wizard 1 & 2 crystallization screen [100 mM HEPES-
608 NaOH pH 7.5, 20% (w/v) PEG 8,000]. Crystal was frozen directly in liquid nitrogen.

609 Selenomethionine-containing crystals (apo structure) were first obtained in solution H5 from
610 NeXtal Cystal Classic II Suite crystallization screen (100 mM succinic acid pH 7.0, 15% (w/v)
611 PEG 3,350). Crystals were reproduced using MRC Maxi 48 well plates with drops composed
612 of equal volumes (1 µL) of protein (at 10 mg mL^{-1} in 20 mM Tris-HCl pH 8.0, 100 mM NaCl,
613 1 mM DTT) and crystallization solution (200 mM succinic acid pH 7.0, 10% (w/v) PEG 3,350)
614 equilibrated against 150 µL reservoir. Crystals were cryo-protected with a 1:1 mixture of
615 Paratone N and Mineral oil before flash freezing in liquid nitrogen.
616 The RmlT/TDP-rhamnose (Thymidine-5'-diphosphate-L-rhamnose disodium, Biosynth Ltd,
617 UK) structure was determined from soaking a crystal obtained in 100 mM Bis-Tris Propane
618 pH 7.0, 200 mM K/Na tartrate tetrahydrate, 20% (w/v) PEG 3,350 (originally identified in
619 condition F9 from PACT premier (Molecular Dimensions). Before freezing, 0.5 µL of a
620 solution containing 55 mM Bis-Tris propane pH 7.0, 110 mM K/Na tartrate tetrahydrate,
621 13.75% (w/v) PEG 3,350, 5% (v/v) glycerol, 25 mM $MgCl_2$ and 30 mM TDP-rhamnose was
622 added to the crystal drop and allowed to equilibrate for 50 min. After quickly transferring the
623 crystal into a solution containing 220 mM K/Na tartrate tetrahydrate, 110 mM Bis-Tris propane
624 pH 7.0, 27.5% (w/v) PEG 3,350, 10% (v/v) glycerol, the crystal was flash-frozen in liquid
625 nitrogen. The structure of $RmlT_{D198A}$ in complex with TDP-rhamnose was determined from a
626 crystal grown in 100 mM Bis-Tris propane pH 7.0, 200 mM K/Na tartrate, 22.5% (w/v) PEG
627 3,350. Crystal was transferred to a 0.5 µL of reservoir solution and then 0.5 µL of 55 mM Bis-
628 Tris propane pH 7.0, 110 mM K/Na tartrate tetrahydrate, 16.75% (w/v) PEG 3,350, 20 mM
629 $MgCl_2$, 20 mM TDP-rhamnose was added. The mixture was allowed to equilibrate for 6 min.
630 Cryoprotection was achieved by adding 0.8 µL of a solution containing 110 mM Bis-Tris
631 propane pH 7.0, 220 mM K/Na tartrate tetrahydrate, 33.5% (w/v) PEG 3,350 prior to flash-
632 freezing in liquid nitrogen. Finally, RmlT crystals were also obtained in condition H6 of the
633 NeXtal Classics Lite Suite crystallization screen (100 mM Tris-HCl pH 8.5, 200 mM sodium
634 acetate., 15% (w/v) PEG 4,000). A crystal grown in this condition was used to solve the
635 RmlT/UDP-glucose structure. Crystal was sequentially transferred to solutions with increasing
636 concentration of DMSO and supplemented with UDP-glucose (110 mM Tris-HCl pH 8.5, 220
637 mM sodium acetate, 16.5% (w/v) PEG 4,000, 10 to 30% DMSO, 5 mM MgCl2, 5 mM UDP-
638 glucose) before flash-freezing in liquid nitrogen.
639 The <u>RmlT structure with bound synthetic 3RboP-$(CH_2)_6NH_2$</u> was obtained from a crystal
640 grown with equal volumes (1 µL) of RmlT protein solution (at 10 mg mL^{-1} in 20 mM Tris-HCl
641 pH 8.0, 100 mM NaCl, 1 mM DTT, 5 mM $MgCl_2$ and with 4 mM 3RboP-$(CH_2)_6NH_2$) and
642 crystallization solution (100 mM MES pH 6.5, 150 mM K/Na tartrate tetrahydrate, 20% (w/v)

643 PEG 3,350) equilibrated against 40 µL reservoir solution. The crystal was transferred to 0.5 µL
644 of crystallization solution and 0.5 uL was added of a solution containing 99 mM MES pH 6.5,
645 148.5 mM K/Na tartrate tetrahydrate, 19.8% (w/v) PEG 3,350, 18% glycerol, 5 mM 3RboP-
646 $(CH_2)_6NH_2$ and 5 mM $MgCl_2$ before flash freezing in liquid nitrogen. The RmlT structure with
647 bound synthetic 4RboP-$(CH_2)_6NH_2$ was obtained from a crystal grown with equal volumes (1
648 µL) of RmlT protein solution (at 10 mg mL^{-1} in 20 mM Tris-HCl pH 8.0, 100 mM NaCl, 1 mM
649 DTT, 5 mM $MgCl_2$ and with 4 mM 4RboP-$(CH_2)_6NH_2$) and crystallization solution (100 mM
650 Bis-Tris propane pH7.0, 200 mM K/Na tartrate tetrahydrate, 17.5% (w/v) PEG 3,350)
651 equilibrated against 40 µL reservoir solution. The crystal was cryo-protected with a 1:1 mixture
652 of Paratone N and Mineral oil before flash-freezing in liquid nitrogen.
653
654 **Data collection and processing**
655 Diffraction data were collected from cryo-cooled (100 K) single crystals with a ~0.98 Å
656 wavelength X-ray beam at beamlines PROXIMA-1 and PROXIMA-2A of the French National
657 Synchrotron Facility (SOLEIL, Gif-sur-Yvette, France) and XALOC of ALBA (Barcelona,
658 Spain). Data sets were processed with XDS [45] and reduced with utilities from the CCP4
659 program suite [46]. X-ray diffraction data statistics are summarized in Table 1.
660
661 **Structure determination, model building and refinement**
662 The structure of apo RmlT was solved by single-wavelength anomalous diffraction (SAD),
663 using the anomalous signal of the selenium at the *K*-absorption edge and pipelines from CCP4
664 package [46]: the SHELXC/SHELXD/SHELXE pipeline [47] was used for Se atom location,
665 the Phaser SAD pipeline [48, 49] for density modification and automatic model building and
666 the Buccaneer pipeline [50, 51] used for automatic model building and refinement. All the
667 other structures were solved by molecular replacement with Phaser [48] using chain A of the
668 apo structure as a search model. Alternating cycles of model building with Coot [52] and
669 refinement with PHENIX [53] were performed until model completion. Simulated annealing
670 was performed once for structures solved by molecular replacement. NCS restrains were used
671 only in the first cycles of refinement. TLS refinement was performed in more advanced stages
672 of refinement, with TLS groups identified automatically by PHENIX. Refined coordinates and
673 structure factors were deposited at the Protein Data Bank [54]. The PDB accession codes 8BZ4,
674 8BZ5, 8BZ6, 8BZ7, 8BZ8, 9GZJ and 9GZK were assigned to apo RmlT, apo RmlT with
675 HEPES, RmlT in complex with UDP-glucose, RmlT in complex with TDP-rhamnose, and
676 $RmlT_{D198A}$ in complex with TDP-rhamnose, RmlT in complex with 3-RboP-(CH2)6NH2 and

677 RmlT in complex with 4-RboP-$(CH_2)_6NH_2$, respectively. Refinement statistics are summarized
678 in Table 1.
679
680 **Analysis of crystallographic structures**
681 The crystallographic models were superposed with SUPERPOSE [46, 55] and secondary
682 structure elements were identified with PROMOTIF [56]. The surface electrostatic potential
683 was calculated with APBS [57] using the AMBER force field [58]. Figures depicting molecular
684 models were created with PyMOL (Schrödinger).
685
686 **Isothermal titration calorimetry**
687 Recombinant RmlT was dialysed overnight against 20 mM HEPES pH 8.0, 100 mM NaCl, 5
688 mM $MgCl_2$. Solution of 200 µM TDP, TDP-rhamnose, TDP-glucose or UDP-glucose
689 (calorimetric syringe) were titrated into 20 µM RmlT (sample cell), with an initial injection of
690 2 µL, followed by 28 injections of 10 µL. Titrations were performed in a MicroCal VP-ITC
691 instrument (GE Healthcare) at 15°C. Data were visualized and analyzed with Origin 7 Software
692 using a single-site binding model.
693
694 **Analytical size-exclusion chromatography**
695 Analytical size-exclusion chromatography was performed on a Superdex 200 10/300 GL
696 column (GE Healthcare) pre-equilibrated with protein storage buffer. Blue dextran (2,000
697 kDa), Ferritin (440 kDa), Aldolase (158 kDa), Ovalbumin (43 kDa) and Ribonuclease A (13.7
698 kDa) were used as standards for column calibration. The K_{av} *versus* Log molecular weight was
699 calculated using the equation $K_{av} = (V_e - V_0)/(V_t - V_0)$, where V_e is the elution volume of
700 the protein, V_0 is the void volume of the column and V_t is the column bed volume.
701
702 ***Listeria monocytogenes* strains**
703 We previously generated the *L. monocytogenes* strains EGDe Δ*rmlT*, EGDe Δ*rmlT*::*rmlT* [13]
704 and EGDe Δ*rmlT*Δl*mo1079* [16]. To generate the *L. monocytogenes* strains EGDe
705 Δ*rmlT*::*rmlT*$_{D198A}$, EGDe Δ*rmlT*::*rmlT*$_{D197A}$, EGDe Δ*rmlT*::*rmlT*$_{W89A}$, EGDe
706 Δ*rmlT*::*rmlT*$_{W223A}$, EGDe Δ*rmlT*::*rmlT*$_{Y368A+E372A}$ and EGDe Δ*rmlT*::*rmlT*$_{Y347A+Y368A+E372A}$
707 strains, the pPL2-derivative plasmids described above were introduced into *E. coli* S17–1 and
708 transferred to the *L. monocytogenes* EGDe Δ*rmlT* strain by conjugation on Brain Heart Infusion
709 (BHI) agar. Transconjugant clones were selected in BHI supplemented with chloramphenicol/

710 colistin/nalidixic acid (Cm/Col/Nax) and chromosomal integration of the plasmids confirmed
711 by PCR and sequencing.
712
713 **Quantitative proteomics analysis**
714 To quantify the level of RmlT in the different *L. monocytogenes* mutants, cytosolic proteomes
715 were isolated. Bacteria cultures growing in BHI were harvested at late exponential growth
716 phase ($OD_{600nm} \approx 0,8$) by centrifugation (4 000 xg for 10 min) and bacterial cells washed twice
717 in lysis buffer (50 mM Tris-HCl (pH 7.5), 1 % SDS and Protease Inhibitor Cocktail
718 (cOmplete™, Roche). Bacteria were mechanically lysed by bead beating in a FastPrep
719 apparatus (45 s, speed 6.5 three cycles) and centrifuged at 20 000 xg for 30 min to remove
720 cellular debris. Supernatant containing the cytosolic soluble proteins was recovered and total
721 protein was quantified using the Bradford method. Each sample was processed for proteomic
722 analysis following the solid-phase-enhanced sample-preparation (SP3) protocol and
723 enzymatically digested with Trypsin/LysC as previously described [59]. Protein identification
724 and quantitation was performed by nanoLC-MS/MS equipped with a Field Asymmetric Ion
725 Mobility Spectrometry - FAIMS interface. This equipment is composed of a Vanquish Neo
726 liquid chromatography system coupled to an Eclipse Tribrid Quadrupole, Orbitrap, Ion Trap
727 mass spectrometer (Thermo Scientific, San Jose, CA). 250 nanograms of peptides of each
728 sample were loaded onto a trapping cartridge (PepMap Neo C18, 300 µm x 5 mm i.d., 174500,
729 Thermo Scientific, Bremen, Germany). Next, the trap column was switched in-line to a µPAC
730 Neo 50 cm column (COL-nano050NeoB) coupled to an EASY-Spray nano flow emitter with
731 10 µm i.d. (ES993, Thermo Scientific, Bremen, Germany). A 130 min separation was achieved
732 by mixing A: 0.1% FA and B: 80% ACN, 0.1% FA with the following gradient at a flow of
733 750 nL/min: 0.1 min (1% B to 4% B) and 1.9 min (4% B to 7% B). Next, the flow was reduced
734 to 250 nL/min with the following gradient: 0.1 min (7.0 to 7.1% B), 80 min (7.1% B to 22.5%
735 B), 30 min (22.5% B to 40% B), 8 min (40%B to 99% B) and 9.9 min at 99% B. Subsequently,
736 the column was equilibrated with 1% B. Data acquisition was controlled by Xcalibur 4.6 and
737 Tune 4.0.4091 software (Thermo Scientific, Bremen, Germany). MS results were obtained
738 following a Data Dependent Acquisition - DDA procedure. MS acquisition was performed with
739 the Orbitrap detector at 120 000 resolution in positive mode, quadrupole isolation, scan range
740 (m/z) 375-1500, RF Lens 30%, standard AGC target, maximum injection time was set to auto,
741 1 microscan, data type profile and without source fragmentation. FAIMS mode: standard
742 resolution, total carrier gas flow: static 4L/min, FAIMS CV: -45, -60 and -75 (cycle time, 1 s).

743 Internal Mass calibration: Run-Start Easy-IC. Filters: MIPS, monoisotopic peak determination:
744 peptide, charge state: 2-7, dynamic exclusion 30s, intensity threshold, 5.0e3. MS/MS data
745 acquisition parameters: quadrupole isolation window 1.8 (m/z), activation type: HCD (30%
746 CE), detector: ion trap, IT scan rate: rapid, mass range: normal, scan range mode: auto,
747 normalized AGC target 100%, maximum injection time: 35 ms, data type centroid. The raw
748 data were processed using the Proteome Discoverer 3.1.0.638 software (Thermo Scientific)
749 and searched against the UniProt database for the *Listeria monocytogenes* EGDe Proteome
750 (2024_02 with 2,844 entries). A common protein contaminant list from MaxQuant was also
751 included in the analysis. The Sequest HT search engine was used to identify tryptic peptides.
752 The ion mass tolerance was 10 ppm for precursor ions and 0.5 Da for fragment ions. The
753 maximum allowed missing cleavage sites was set to two. Cysteine carbamidomethylation was
754 defined as constant modification. Methionine oxidation, deamidation of glutamine and
755 asparagine, peptide terminus glutamine to pyroglutamate, and protein N-terminus acetylation,
756 Met-loss, and Met-loss+acetyl were defined as variable modifications. Peptide confidence was
757 set to high. The processing node Percolator was enabled with the following settings: maximum
758 delta Cn 0.05; target FDR (strict) was set to 0.01 and target FDR (relaxed) was set to 0.05,
759 validation based on q-value. Protein label-free quantitation was performed with the Minora
760 feature detector node at the processing step. Precursor ions quantification was performed at the
761 consensus step with the following parameters: unique plus razor peptides were included,
762 precursor abundance based on intensity, and normalization based on total peptide amount. For
763 hypothesis testing, protein ratio calculation was pairwise ratio-based and an t-test (background
764 based) hypothesis test was performed.
765
766 **Isolation and purification of wall teichoic acids**
767 WTAs from *L. monocytogenes* strains wild-type, Δ*rmlT*, Δ*lmo1079* and Δ*rmlT*Δ*lmo1079*, were
768 isolated and purified as previously described [60] with some modifications. *L. monocytogenes*
769 cells grown overnight in 20 mL BHI at 37°C were collected by centrifugation at 4,000xg for
770 10 min. Cells were washed once in buffer 1 (50 mM MES pH 6.5), resuspended in buffer 2 (50
771 mM MES pH 6.5, 4% (w/v) SDS), and boiled in a water bath for 1 h. Cell debris was collected
772 by centrifugation at 4,000xg for 10 min and resuspended in 2 mL of buffer 1. The pellet was
773 washed sequentially in 1 ml of buffers 2, 3 [50 mM MES pH 6.5, 2% (w/v) NaCl] and 1.
774 Washed pellet was resuspended in 1 mL of 20 mM Tris-HCl pH 8.0, 0.5% (w/v) SDS, 20 µg
775 proteinase K and incubated at 50°C for 4 h with agitation (1,400 rpm). To remove SDS, the

776 sample was centrifuged at 16,000xg for 1 min and washed once with buffer 3 and three times
777 with distilled H_2O. Sample was then resuspended in 1 mL of 0.1 M NaOH and shaken at room
778 temperature for 16 h. The remaining insoluble cell debris was removed by centrifugation at
779 16,000xg for 10 min and the supernatant containing the hydrolysed crude WTAs was
780 neutralized with 1 M Tris-HCl pH 7.8. The sample was dialyzed against distilled H_2O using a
781 1 kDa cut-off membrane. Finally, isolated crude WTAs were lyophilized and resuspended in
782 ultra-pure H_2O to a final concentration of 10 mg mL^{-1} (considering ribitol monomer molecular
783 weight) [60].
784
785 **RmlT activity assay**
786 The activity of RmlT variants was analyzed using the Glycosyltransferase Activity Kit (R&D
787 Systems) according to the manufacturer's protocol. Recombinant RmlT (2 μM), was incubated
788 with wild-type WTAs, containing both GlcNAc and rhamnose modifications (wild-type WTAs
789 purified from the *L. monocytogenes* strains EGDe); WTAs containing only GlcNAc
790 modification (WTAs- GlcNAc purified from EGDe Δ*rmlT*); WTAs containing only rhamnose
791 modification (WTAs-rhamnose purified from EGDe Δ*lmo1079*); and naked WTAs without
792 any glycosylation (naked WTAs purified from EGDe Δ*rmlT*Δ*lmo1079*) (1 mM) and TDP-
793 rhamnose, UDP-rhamnose or UDP-glucose (200 μM) in reaction buffer (5 mM $MgCl_2$, 25 mM
794 Tris, 10 mM $CaCl_2$, pH 7.5) at 37°C for 30 min. In the metal bridge coordination experiment
795 with $RmlT_{W145C+A472C}$, the enzyme (2 μM) was incubated with naked WTAs (1 mM) and TDP-
796 rhamnose (200 μM) in reaction buffer (5 mM $MgCl_2$, 25 mM Tris, 10 mM $CaCl_2$, 100 μM
797 TCEP, pH 7.5) at 37°C for 30 min, in presence of absence of $CdCl_2$ (100 μM). Free phosphate
798 released upon hydrolysis of TDP or UDP produced by RmlT was quantified by absorbance at
799 620 nm using a Synergy 2 multi-mode plate reader (BioTek, USA). RmlT reaction mixtures
800 were also separated in 20 % polyacrylamide gels and WTAs were stained with 1 mg mL^{-1}
801 Alcian Blue solution after overnight incubation.
802
803 **Cell wall rhamnose binding assay**
804 Rhamnose present at the bacterial surface was quantified using a bacteriophage receptor
805 binding protein (gp17) fused to GFP (gp17-GFP) (provided by M. Loessner, ETH Zurich). The
806 assay was performed as described before [18]. Briefly, purified gp17-GFP was centrifuged at
807 30,000xg and 4°C for 1 h to remove protein aggregates. Cells from one milliliter of
808 exponentially growing bacterial (OD_{600nm} = 0.5-0.6) were harvested by centrifugation,

809 resuspended in 100 µL of PBS and incubated with 2.4 µg of gp17-GFP at room temperature
810 for 20 min. Cells were washed three times with PBS and binding to the bacterial cell wall was
811 visualized using a fluorescence microscope Olympus BX53 or quantified using a plate reader
812 Synergy 2 (BioTek, USA).
813
814 **Animal infections**
815 Virulence studies were performed in mouse models of BALB/c strain. Infections were
816 performed in six-to-eight week-old specific-pathogen-free females (n=5, except for EGDe
817 Δ*rmlT*::*rmlT* in which n=4) as described [61]. Briefly, intravenous infections were performed
818 through the tail vein with 10^4 CFU of bacteria in PBS. The infection was carried out for 72 h,
819 at which point animals were euthanatized by general anaesthesia. Spleen and liver were
820 aseptically collected, homogenized in sterile PBS, and serial dilutions of the organ
821 homogenates plated in BHI agar. Mice were maintained at the i3S animal facilities, in high
822 efficiency particulate air (HEPA) filter-bearing cages under 12 h light cycles, and were given
823 sterile chow and autoclaved water *ad libitum*. All animal procedures were performed in
824 agreement with the guidelines of the European Commission for the handling of laboratory
825 animals (directive 2010/63/EU), the Portuguese legislation for the use of animals for scientific
826 purposes (Decreto-Lei 113/2013), and were approved by the i3S Animal Ethics Committee as
827 well as by the Direcção Geral de Veterinária (the Portuguese authority for animal protection)
828 under licenses 2017-06-30 015302 and 2023-04-05 006564.
829
830 **Statistical analyses**
831 Statistical analyses were calculated using the software Prism 9 (GraphPad Software). Unpaired
832 two-tailed Student's t-test was used to compare the means of two groups; one-way ANOVA
833 was used with Tukey's post-hoc test for pairwise comparison of means from more than two
834 groups, or with Dunnett's post-hoc test for comparison of means relative to the mean of a
835 control group. Differences with a calculated *p*-value above 0.05 were considered non-
836 significant and statistically significant differences were noted as follows: * = $p < 0.05$; ** = p
837 < 0.01; *** = $p < 0.001$; **** = p <0,0001.
838
839 **Supplementary Materials:** Supplementary Figure 1: Structure of *L. monocytogenes* RmlT and
840 *S. aureus* TarS, TarP. Supplementary Figure 2: Amino-acid sequence alignment of RmlT, TarS
841 and TarP. Supplementary Figure 3: Properties of RmlT. Supplementary Figure 4: Electron
842 density map of the donor substrates TDP-rhamnose and UDP-glucose in different forms of

843 RmlT. Supplementary Figure 5: Active site of RmlT with TDP-rhamnose or UDP-glucose.
844 Supplementary Figure 6: Omit map of the donor substrate TDP-rhamnose in different RmlT
845 copies. Supplementary Figure 7: Active sites of RmlT, TarS and TarP. Supplementary Figure
846 8: Active site of RmlT with and without TDP-rhamnose. Supplementary Figure 9: Omit map
847 of the donor substrate TDP-rhamnose in different $RmlT_{D198A}$ copies. Supplementary Figure 10:
848 Omit map of the donor substrate UDP-glucose in different RmlT copies. Supplementary Figure
849 11: Omit map of 3-RboP in different copies of RmlT. Supplementary Figure 12: Omit map of
850 the 4-RboP in different copies of RmlT. Supplementary Figure 13: HEPES binding sites.
851 Supplementary Figure 14: Quantification of RmlT protein abundance in *L. monocytogenes*
852 lysates. Supplementary Table 1: Quality of fit of protein chains to electron-density map.
853 Supplementary Table 2: Bacterial strains and plasmids. Supplementary Table 3: Primer
854 sequences.
855
856 **Author's contributions:** RM, JMC and DC conceptualize the overarching aims of the research
857 study. RM, TBC, RP, TV, JDC-C, SS, JMC and DC conceived and designed the experiments.
858 RM, TBC, TV and RP performed the experiments and data acquisition. RM, TBC, RP, SS,
859 JMC and DC analysed and interpreted the data. JM-C and DC had management as well as
860 coordination responsibility for the execution of the research work. JDC-C, JM-C and DC
861 contributed to the acquisition of the financial supports and resources leading to this publication.
862 All authors contributed to the drafting of some parts of the manuscript, including reading and
863 revising critically the manuscript for important intellectual content, as well as approval of the
864 final version.
865
866 **Competing interests:** All authors have declared no competing interests.
867
868 **Acknowledgments:** The work leading to these results was supported by FEDER – "Fundo
869 Europeu de Desenvolvimento Regional" funds through the NORTE 2020 - Norte Portugal
870 Regional Operational Programme, Portugal 2020, and by Portuguese funds through FCT -
871 Fundação para a Ciência e a Tecnologia/Ministério da Ciência, Tecnologia e Ensino Superior
872 in the framework of the project NORTE-01-0145-FEDER-030020 and PTDC/SAU-
873 INF/30020/2017, and by the "la Caixa" Foundation and FCT, I.P. under project CI21-00035
874 and LCF/PR/ HR23-00682. TBC was supported by FCT (2021.01203.CEECIND).
875 The authors acknowledge the SOLEIL and ALBA synchrotrons for access and thank their staff
876 for help with data collection. Support from the Biochemical and Biophysical Technologies,

Animal Facility, Proteomics and X-ray Crystallography scientific platforms of i3S (Porto, Portugal) is also acknowledged. The authors extend their appreciation to Martin J. Loessner from ETH Zurich (Switzerland) that kindly provided the gp17-GFP recombinant construct.

881 **References**

882 1. ECDC, *Listeriosis*, in *ECDC. Annual Epidemiological Report*. 2023.
883 2. ECDC, *The European Union One Health 2021 Zoonoses Report.* 2022.
884 3. Brown, S., J.P. Santa Maria, Jr., and S. Walker, *Wall teichoic acids of gram-positive*
885 *bacteria.* Annu Rev Microbiol, 2013. **67**: p. 313-36.
886 4. Sumrall, E.T., et al., *Structure and function of Listeria teichoic acids and their*
887 *implications.* Molecular microbiology, 2020. **113**(3): p. 627-637.
888 5. Percy, M.G. and A. Grundling, *Lipoteichoic acid synthesis and function in gram-*
889 *positive bacteria.* Annu Rev Microbiol, 2014. **68**: p. 81-100.
890 6. Rismondo, J., M.G. Percy, and A. Grundling, *Discovery of genes required for*
891 *lipoteichoic acid glycosylation predicts two distinct mechanisms for wall teichoic acid*
892 *glycosylation.* J Biol Chem, 2018. **293**(9): p. 3293-3306.
893 7. Percy, M.G., et al., *Identification of a Lipoteichoic Acid Glycosyltransferase Enzyme*
894 *Reveals that GW-Domain-Containing Proteins Can Be Retained in the Cell Wall of Listeria*
895 *monocytogenes in the Absence of Lipoteichoic Acid or Its Modifications.* J Bacteriol, 2016.
896 **198**(15): p. 2029-42.
897 8. Uchikawa, K., I. Sekikawa, and I. Azuma, *Structural studies on lipoteichoic acids from*
898 *four Listeria strains.* Journal of Bacteriology, 1986. **168**(1): p. 115-22.
899 9. Promadej, N., et al., *Cell wall teichoic acid glycosylation in Listeria monocytogenes*
900 *serotype 4b requires gtcA, a novel, serogroup-specific gene.* Journal of Bacteriology, 1999.
901 **181**(2): p. 418-25.
902 10. Swaminathan, B. and P. Gerner-Smidt, *The epidemiology of human listeriosis.*
903 Microbes Infect, 2007. **9**(10): p. 1236-43.
904 11. Sumrall, E.T., et al., *Glycotyping and Specific Separation of Listeria monocytogenes*
905 *with a Novel Bacteriophage Protein Tool Kit.* Applied and environmental microbiology, 2020.
906 **86**(13).
907 12. Carvalho, F., S. Sousa, and D. Cabanes, *How Listeria monocytogenes organizes its*
908 *surface for virulence.* Front Cell Infect Microbiol, 2014. **4**: p. 48.
909 13. Carvalho, F., et al., *L-Rhamnosylation of Listeria monocytogenes Wall Teichoic Acids*
910 *Promotes Resistance to Antimicrobial Peptides by Delaying Interaction with the Membrane.*
911 PLoS Pathog, 2015. **11**(5): p. e1004919.
912 14. Carvalho, F., S. Sousa, and D. Cabanes, *l-Rhamnosylation of wall teichoic acids*
913 *promotes efficient surface association of Listeria monocytogenes virulence factors InlB and*
914 *Ami through interaction with GW domains.* Environmental microbiology, 2018. **20**(11): p.
915 3941-3951.
916 15. Spears, P.A., et al., *Listeria monocytogenes wall teichoic acid decoration in virulence*
917 *and cell-to-cell spread.* Mol Microbiol, 2016. **101**(5): p. 714-30.
918 16. Meireles, D., et al., *Listeria monocytogenes Wall Teichoic Acid Glycosylation*
919 *Promotes Surface Anchoring of Virulence Factors, Resistance to Antimicrobial Peptides, and*
920 *Decreased Susceptibility to Antibiotics.* Pathogens (Basel, Switzerland), 2020. **9**(4).
921 17. Sumrall, E.T., et al., *Phage resistance at the cost of virulence: Listeria monocytogenes*
922 *serovar 4b requires galactosylated teichoic acids for InlB-mediated invasion.* PLoS pathogens,
923 2019. **15**(10): p. e1008032.
924 18. Bielmann, R., et al., *Receptor binding proteins of Listeria monocytogenes*
925 *bacteriophages A118 and P35 recognize serovar-specific teichoic acids.* Virology, 2015. **477**:
926 p. 110-118.
927 19. Faith, N., et al., *The role of L. monocytogenes serotype 4b gtcA in gastrointestinal*
928 *listeriosis in A/J mice.* Foodborne Pathog Dis, 2009. **6**(1): p. 39-48.
929 20. Shen, Y., et al., *Structural and functional diversity in Listeria cell wall teichoic acids.*
930 J Biol Chem, 2017. **292**(43): p. 17832-17844.

931 21. Cheng, Y., et al., *Teichoic acid glycosylation mediated by gtcA is required for phage*
932 *adsorption and susceptibility of Listeria monocytogenes serotype 4b.* Applied &
933 Environmental Microbiology, 2008. **74**(5): p. 1653-5.
934 22. Xia, G., et al., *Glycosylation of wall teichoic acid in Staphylococcus aureus by TarM.*
935 J Biol Chem, 2010. **285**(18): p. 13405-15.
936 23. Brown, S., et al., *Methicillin resistance in Staphylococcus aureus requires glycosylated*
937 *wall teichoic acids.* Proc Natl Acad Sci U S A, 2012. **109**(46): p. 18909-14.
938 24. Gerlach, D., et al., *Methicillin-resistant Staphylococcus aureus alters cell wall*
939 *glycosylation to evade immunity.* Nature, 2018. **563**(7733): p. 705-709.
940 25. Guo, Y., et al., *Cell wall glycosylation in Staphylococcus aureus: targeting the tar*
941 *glycosyltransferases.* Curr Opin Struct Biol, 2021. **68**: p. 166-174.
942 26. Sobhanifar, S., et al., *Structure and mechanism of Staphylococcus aureus TarM, the*
943 *wall teichoic acid alpha-glycosyltransferase.* Proceedings of the National Academy of
944 Sciences of the United States of America, 2015. **112**(6): p. E576-85.
945 27. Sobhanifar, S., et al., *Structure and Mechanism of Staphylococcus aureus TarS, the*
946 *Wall Teichoic Acid beta-glycosyltransferase Involved in Methicillin Resistance.* PLoS
947 pathogens, 2016. **12**(12): p. e1006067.
948 28. Camejo, A., et al., *In vivo transcriptional profiling of Listeria monocytogenes and*
949 *mutagenesis identify new virulence factors involved in infection.* PLoS Pathog, 2009. **5**(5): p.
950 e1000449.
951 29. Rismondo, J., et al., *GtcA is required for LTA glycosylation in Listeria monocytogenes*
952 *serovar 1/2a and Bacillus subtilis.* Cell Surf, 2020. **6**: p. 100038.
953 30. Chhetri, G., P. Kalita, and T. Tripathi, *An efficient protocol to enhance recombinant*
954 *protein expression using ethanol in Escherichia coli.* MethodsX, 2015. **2**: p. 385-91.
955 31. Puljung, M.C. and W.N. Zagotta, *Labeling of specific cysteines in proteins using*
956 *reversible metal protection.* Biophys J, 2011. **100**(10): p. 2513-21.
957 32. Martinez, O.E., et al., *Insight into the molecular basis of substrate recognition by the*
958 *wall teichoic acid glycosyltransferase TagA.* J Biol Chem, 2022. **298**(2): p. 101464.
959 33. van der Es, D., et al., *Teichoic acids: synthesis and applications.* Chemical Society
960 Reviews, 2017. **46**(5): p. 1464-1482.
961 34. Winstel, V., G. Xia, and A. Peschel, *Pathways and roles of wall teichoic acid*
962 *glycosylation in Staphylococcus aureus.* Int J Med Microbiol, 2014. **304**(3-4): p. 215-21.
963 35. Weidenmaier, C., et al., *Role of teichoic acids in Staphylococcus aureus nasal*
964 *colonization, a major risk factor in nosocomial infections.* Nat Med, 2004. **10**(3): p. 243-5.
965 36. Brown, S., Y.H. Zhang, and S. Walker, *A revised pathway proposed for Staphylococcus*
966 *aureus wall teichoic acid biosynthesis based on in vitro reconstitution of the intracellular steps.*
967 Chem Biol, 2008. **15**(1): p. 12-21.
968 37. Eugster, M.R., et al., *Bacteriophage predation promotes serovar diversification in*
969 *Listeria monocytogenes.* Mol Microbiol, 2015. **97**(1): p. 33-46.
970 38. Rismondo, J. and L.M. Schulz, *Not Just Transporters: Alternative Functions of ABC*
971 *Transporters in Bacillus subtilis and Listeria monocytogenes.* Microorganisms, 2021. **9**(1).
972 39. Gerlach, D., et al., *Methicillin-resistant Staphylococcus aureus alters cell wall*
973 *glycosylation to evade immunity.* Nature, 2018. **563**(7733): p. 705-709.
974 40. Hort, M., et al., *The Role of beta-Glycosylated Wall Teichoic Acids in the Reduction of*
975 *Vancomycin Susceptibility in Vancomycin-Intermediate Staphylococcus aureus.* Microbiol
976 Spectr, 2021. **9**(2): p. e0052821.
977 41. Smith, R.E., et al., *Decoration of the enterococcal polysaccharide antigen EPA is*
978 *essential for virulence, cell surface charge and interaction with effectors of the innate immune*
979 *system.* PLoS pathogens, 2019. **15**(5): p. e1007730.

42. Dale, J.L., et al., *Multiple roles for Enterococcus faecalis glycosyltransferases in biofilm-associated antibiotic resistance, cell envelope integrity, and conjugative transfer.* Antimicrob Agents Chemother, 2015. **59**(7): p. 4094-105.
43. Klock, H.E. and S.A. Lesley, *The Polymerase Incomplete Primer Extension (PIPE) method applied to high-throughput cloning and site-directed mutagenesis.* Methods Mol Biol, 2009. **498**: p. 91-103.
44. Guo, Y., et al., *Invasive Staphylococcus epidermidis uses a unique processive wall teichoic acid glycosyltransferase to evade immune recognition.* Sci Adv, 2023. **9**(47): p. eadj2641.
45. Kabsch, W., *XDS.* (1399-0047 (Electronic)).
46. Winn, M.D., et al., *Overview of the CCP4 suite and current developments.* (1399-0047 (Electronic)).
47. Sheldrick, G.M., *Experimental phasing with SHELXC/D/E: combining chain tracing with density modification.* (1399-0047 (Electronic)).
48. McCoy, A.J., et al., *Phaser crystallographic software.* J Appl Crystallogr, 2007. **40**(Pt 4): p. 658-674.
49. Cowtan, K., *Recent developments in classical density modification.* (1399-0047 (Electronic)).
50. Cowtan, K., *The Buccaneer software for automated model building. 1. Tracing protein chains.* (0907-4449 (Print)).
51. Kovalevskiy, O., et al., *Overview of refinement procedures within REFMAC5: utilizing data from different sources.* (2059-7983 (Electronic)).
52. Emsley, P., et al., *Features and development of Coot.* (1399-0047 (Electronic)).
53. Adams, P.D., et al., *PHENIX: a comprehensive Python-based system for macromolecular structure solution.* (1399-0047 (Electronic)).
54. Berman, H.M., et al., *The Protein Data Bank.* (0305-1048 (Print)).
55. Krissinel, E. and K. Henrick, *Secondary-structure matching (SSM), a new tool for fast protein structure alignment in three dimensions.* Acta Crystallogr D Biol Crystallogr, 2004. **60**(Pt 12 Pt 1): p. 2256-68.
56. Hutchinson, E.G. and J.M. Thornton, *PROMOTIF--a program to identify and analyze structural motifs in proteins.* Protein Sci, 1996. **5**(2): p. 212-20.
57. Baker, N.A., et al., *Electrostatics of nanosystems: application to microtubules and the ribosome.* Proc Natl Acad Sci U S A, 2001. **98**(18): p. 10037-41.
58. Cornell, W.D., et al., *A Second Generation Force Field for the Simulation of Proteins, Nucleic Acids, and Organic Molecules.* Journal of the American Chemical Society, 1995. **117**(19): p. 5179-5197.
59. Osorio, H., et al., *Proteomics Analysis of Gastric Cancer Patients with Diabetes Mellitus.* J Clin Med, 2021. **10**(3).
60. Carvalho, F., et al., *Extraction of cell wall-bound teichoic acids and surface proteins from Listeria monocytogenes.* Methods Mol Biol, 2013. **966**: p. 289-308.
61. Cabanes, D., M. Lecuit, and P. Cossart, *Animal models of Listeria infection.* Curr Protoc Microbiol, 2008. **Chapter 9**: p. Unit9B 1.